



HAL
open science

Calibration of accelerometers aboard GRACE satellites by comparison with POD-based nongravitational accelerations

Ales Bezdek

► **To cite this version:**

Ales Bezdek. Calibration of accelerometers aboard GRACE satellites by comparison with POD-based nongravitational accelerations. *Journal of Geodynamics*, 2010, 50 (5), pp.410. 10.1016/j.jog.2010.05.001 . hal-00688184

HAL Id: hal-00688184

<https://hal.science/hal-00688184v1>

Submitted on 17 Apr 2012

HAL is a multi-disciplinary open access archive for the deposit and dissemination of scientific research documents, whether they are published or not. The documents may come from teaching and research institutions in France or abroad, or from public or private research centers.

L'archive ouverte pluridisciplinaire **HAL**, est destinée au dépôt et à la diffusion de documents scientifiques de niveau recherche, publiés ou non, émanant des établissements d'enseignement et de recherche français ou étrangers, des laboratoires publics ou privés.

Accepted Manuscript

Title: Calibration of accelerometers aboard GRACE satellites
by comparison with POD-based nongravitational accelerations

Author: Ales Bezdek

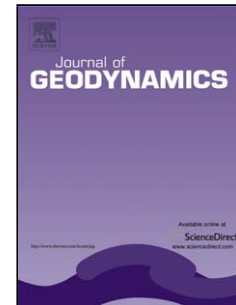
PII: S0264-3707(10)00087-6
DOI: doi:10.1016/j.jog.2010.05.001
Reference: GEOD 1003

To appear in: *Journal of Geodynamics*

Received date: 19-11-2009
Revised date: 4-5-2010
Accepted date: 9-5-2010

Please cite this article as: Bezdek, A., Calibration of accelerometers aboard GRACE satellites by comparison with POD-based nongravitational accelerations, *Journal of Geodynamics* (2008), doi:10.1016/j.jog.2010.05.001

This is a PDF file of an unedited manuscript that has been accepted for publication. As a service to our customers we are providing this early version of the manuscript. The manuscript will undergo copyediting, typesetting, and review of the resulting proof before it is published in its final form. Please note that during the production process errors may be discovered which could affect the content, and all legal disclaimers that apply to the journal pertain.



Calibration of accelerometers aboard GRACE satellites by comparison with POD-based nongravitational accelerations

Aleš Bezděk*

*Astronomical Institute, Academy of Sciences of the Czech Republic, Fričova 298, 251 65
Ondřejov, Czech Republic*

Abstract

1 The proposed calibration method uses the precise kinematic positions derived
2 from the data of the GPS receivers aboard the twin GRACE satellites (POD, Pre-
3 cise Orbit Determination). The total satellite accelerations are obtained numeri-
4 cally as a second derivative of the kinematic positions, from these the modelled
5 forces of gravitational origin are subtracted. The resulting nongravitational ac-
6 celerations then serve as a calibration standard for the uncalibrated accelerometer
7 data. The calibration parameters for the GRACE accelerometers have already
8 been published using other methods. The aim of our study was to obtain not only
9 the calibrated accelerometer measurements, but also a statistically correct estimate
10 of their uncertainty.

11 The main problem in the application of a numerical derivative to observational
12 data is the amplification of noise, especially at high frequencies. Besides, the
13 filter of the numerical derivative introduces the correlation structure in the noise,
14 which complicates the uncertainty estimates using the ordinary least squares. We
15 succeeded in solving both of these problems by using the generalized least squares
16 (GLS) method.

*Tel.: +420 323620232, fax: +420 323620117.
Preprint submitted to Journal of Geodynamics
Email address: bezdek@asu.cas.cz (Aleš Bezděk)
URL: <http://www.asu.cas.cz/~bezdek/> (Aleš Bezděk)

May 4, 2010

17 Using the proposed procedure, the calibration parameters for all three ac-
18 celerometer data components were obtained. To remove the serial correlation in
19 the POD positions, we used the GLS method together with a fitted autoregressive
20 process. In this way, a realistic estimate of accuracy of the calibrated accelerom-
21 eter data was obtained for the along-track component. The time evolution of the
22 calibration parameters over a 1.5-year period (08/2002–03/2004) display approx-
23 imately constant scale factors and slowly changing biases for both GRACE A and
24 B satellites, which is in accordance with the results in the references.

Key words: Space accelerometers, Nongravitational forces, Generalized least
squares, Autoregressive processes

25 **1. Introduction**

26 The wealth of quality data from the two GRACE satellites (launched in 2002),
27 and also from its predecessor satellite CHAMP (launched in 2000), has substan-
28 tially contributed to the improved modelling of the global Earth's gravity field, its
29 static part as well as its temporal variations (Reigber et al., 2006; Schmidt et al.,
30 2006). As the orbital altitude of these satellites is very low (below 550 km), they
31 are equipped with space accelerometers, whose purpose is to measure the non-
32 gravitational accelerations. When processing the measurements from the CHAMP
33 and GRACE missions to produce the gravity field models, the measurements from
34 the onboard accelerometers have to be calibrated. The gravity on the ground is so
35 much larger than the nongravitational accelerations measured in space that the
36 electronic properties of a space accelerometer do not allow it to be calibrated be-
37 fore the launch. Many scientific teams using the CHAMP and GRACE data for
38 the gravity field modelling therefore calibrated the accelerometer measurements

39 (Flury et al., 2006; Reigber et al., 2003, 2005a). Ideally, the calibrated accelerom-
40 eter measurements should be accompanied with correct uncertainty estimates, but
41 this is usually impossible, because the accelerometer calibration parameters con-
42 stitute only a tiny part of the fitted parameters. Moreover, to stabilize the solution
43 of large regression equations in the gravity field studies, one must usually use
44 some regularization scheme, but then the regularized solution is biased and the
45 bias could be much larger than the computed confidence intervals (Aster et al.,
46 2005). Over the years it was found that the accelerometer calibration parameters
47 can vary a lot depending on the analysis methods and the context of data usage
48 (Bettadpur, 2004a).

49 Besides the gravity field modelling, the accelerometer measurements may also
50 be used for the analysis of sources of the nongravitational forces themselves, espe-
51 cially for studying problems related to thermospheric density and winds (Doorn-
52 bos et al., 2009; Flury et al., 2008). Specific for the attitude stabilized satellites
53 CHAMP and GRACE are the firings of the attitude control thrusters, which show
54 up in the linear accelerometer measurements, mainly because of thruster misalign-
55 ments (Frommknecht et al., 2006). As real forces, the thruster firings are properly
56 registered by the onboard accelerometers so that the full nongravitational signal
57 can later be eliminated in the gravity field determination; this is one of the reasons
58 why space accelerometers are useful in geodetic missions. However, from the
59 point of view of aeronomy studies, the magnitude of the thruster events is often at
60 the same order as that of the external nongravitational accelerations themselves,
61 especially in the cross-track and radial directions. On the other hand, thermo-
62 spheric density is derived from air drag, which is the dominant nongravitational
63 acceleration in the along-track direction. The use of the properly calibrated ac-

64 celerometer data for aeronomy studies was the main motive for writing this paper.

65 From the several calibration methods currently in use, we chose the satellite
66 acceleration approach. The basic idea of the acceleration approach is to derive
67 satellite accelerations by double numerical differentiation of the satellite positions
68 along the precise orbit. Newton's second law of motion then links the resulting ac-
69 celeration vectors to the forces acting upon the satellite. The successful implemen-
70 tation of this technique with results comparable to the classical, dynamic approach
71 was enabled by the fact that kinematic orbits can nowadays be determined at a few
72 cm accuracy. The satellite acceleration approach has been used by several scien-
73 tific teams for the modelling of the geopotential (e.g., Ditmar et al., 2006; Reubelt
74 et al., 2006; Švehla and Földvary, 2006). Numerically, the accelerometer cali-
75 bration is much simpler compared to the gravity field determination, where one
76 needs an inversion of normal matrix with tens of thousands unknowns and mil-
77 lions of measurements, a difficult computational problem, which requires special
78 techniques to be applied. In this study, the calibration standard, the vector of the
79 POD-based nongravitational acceleration, is projected into the accelerometer ref-
80 erence frame, where each component is directly compared with the uncalibrated
81 accelerometer data and the linear least-squares calibration model may be used. In
82 the ideal case, the residuals should be approximately independent and normally
83 distributed to enable statistical inference concerning the regression results. On the
84 other hand, the acceleration approach has the problem with the amplified noise.
85 The double numerical differentiation increases the noise in the positions propor-
86 tionally to the squared frequency, and, therefore, the high-frequency noise will be
87 amplified very significantly.

88 The prime motivation of this paper is that for a proper use of the accelerometer

89 measurements, and more generally of any observational data, one needs not only
90 the measurement result, a point estimate of the true value, but also an estimate of
91 the uncertainty of the result, a realistic error bar, which is a quantitative statement
92 about where the true value ‘really’ is, with a given probability (cf., Taylor and
93 Kuyatt, 1994). Without error bars it is not possible to assess the quality of obser-
94 vations in question, to compare two competing theories using the observational
95 data, to properly combine measurements from different sources, or to correctly
96 combine the measurements even from the same experiment, if they have noncon-
97 stant variance.

98 **2. Gravitational and nongravitational accelerations**

99 *2.1. GRACE project and SuperSTAR accelerometer*

100 The Gravity Recovery And Climate Experiment (GRACE) is a joint US/German
101 satellite mission (Tapley et al., 2004) designed to very accurately map variations
102 in the Earth’s gravity field. The two almost identical GRACE satellites were
103 launched in March 2002 into a near polar orbit at about 500-km altitude, separated
104 by approximately 200 km. Each spacecraft carries a science payload consisting of
105 microwave ranging system, GPS receiver, star cameras and accelerometer. Based
106 on data from this mission, the most recent global Earth gravitational field models
107 were published (Förste et al., 2008; Pavlis et al., 2008; Tapley et al., 2007).

108 The SuperSTAR accelerometer on board of the GRACE satellites is a three
109 axis capacitive accelerometer with two sensitive and one less sensitive axes. The
110 sensitive axes point in the flight and radial directions, the less sensitive axis points
111 in the cross-track direction. The precision of the sensitive axes is specified to be
112 $10^{-10} \text{ m s}^{-2}$, and that of the less sensitive axis 10^{-9} m s^{-2} , within the bandwidth

113 of 2×10^{-4} – 10^{-1} Hz (Flury et al., 2008). Compared to the CHAMP accelerome-
 114 ter, the GRACE accelerometers have thermally controlled environment with the
 115 temperature variations below 0.1 K/orbit (Tapley and Reigber, 2002).

116 2.2. *Nongravitational accelerations*

117 Figure B.1 shows the simulated nongravitational accelerations acting on the
 118 GRACE A satellite during one orbital revolution. The projection of the accelera-
 119 tion vectors refers to the satellite local reference frame; the three components are
 120 the along-track (A-T; projected to the velocity direction), the cross-track (C-T;
 121 direction of angular momentum) and the radial one (RAD; completes the right-
 122 handed system). The figure is typical for satellites in low Earth orbits (LEO,
 123 altitudes 100–2000 km, mainly 150–800 km): the dominant nongravitational ac-
 124 celerations change with the satellite local reference frame directions; the close-
 125 Earth motion makes the satellite to pass through the Earth’s shadow, which is
 126 visualized by the characteristic jumps. In the along-track component, the main
 127 nongravitational driver is the *atmospheric drag* (DRAG), pointing always in the
 128 direction opposite to the satellite’s motion. Even in the along-track component,
 129 there may appear jumps in the smooth waveform of the drag acceleration caused
 130 by the *direct solar radiation pressure* (DSRP), whose action is dominant in the
 131 sunlit part of the cross-track and radial components. In the shadow of Earth, the
 132 *terrestrial infrared radiation* (IR) dominates the radial component. Sometimes,
 133 when the satellite passes directly below the Sun, also the signal from the *reflected*
 134 *solar radiation* (ALB) may be recognizable in the graphs of the nongravitational
 135 accelerations. In each panel, there is also the sum of the individual simulated non-
 136 gravitational accelerations, $\mathbf{a}_{\text{NG}}^{\text{SIM}}$. The magnitude of the nongravitational forces in
 137 each local reference frame direction depends on the satellite shape and its phys-

138 ical properties; in this study, for the GRACE satellites we used the macro model
139 and surface properties from Bettadpur (2007) and the mass from ISDC/GFZ data
140 centre (<http://isdc.gfz-potsdam.de/grace/>). General formulae for computing the
141 nongravitational accelerations may be found e.g. in Montenbruck and Gill (2001)
142 or Milani et al. (1987), in this study we used the model of neutral thermospheric
143 density DTM-2000 (Bruinsma et al., 2003) and the zonal and seasonal models of
144 the Earth's albedo and emissivity (Knocke et al., 1988).

145 Figure 1 should be positioned here.

146 Figure 2 should be positioned here.

147 Figure B.2 displays the Level-1B accelerometer data of GRACE A during
148 the same period as in Figure B.1. There is an apparent similarity between the
149 waveforms of the sum of the simulated nongravitational accelerations (Fig. B.1)
150 and the uncalibrated accelerometer readouts (Fig. B.2). This is typical for all
151 GRACE Level-1B accelerometer data and provides evidence that the smoother
152 simulated nongravitational accelerations and the accelerometer measurements are
153 consistent with each other. On the other hand, if we compare the units on vertical
154 axes of graphs in Figures B.1 and B.2, it is clear that the accelerometer data are
155 not calibrated; for example, it follows from the geometry of the GRACE A motion
156 during the revolution in question that in the radial component the nongravitational
157 acceleration must pass through zero. In the cross-track and radial components, the

158 sudden spikes in the waveform correspond to the cold-gas thruster firings, which
159 are activated on average every 2.3 minutes by the attitude control system in order
160 to satisfy the pointing requirements of the microwave ranging system (Flury et al.,
161 2008).

162 Figure 3 should be positioned here.

163 2.3. Gravitational vs. nongravitational accelerations

164 The histograms in Figure B.3 show the magnitude of the individual accelera-
165 tions in the satellite local reference frame components. We simulated the or-
166 bital evolution of the GRACE A satellite during 1.5 years, every 60 minutes we
167 recorded the magnitudes of the accelerations acting on the satellite and then draw
168 a histogram for each acceleration. We do not show the specific numbers for the
169 histogram counts on the vertical axis, which is linear, as these are only formal
170 depending on the sampling period and would add complexity to the graphs.

171 The dominant acceleration is due to the static gravitational field; the accel-
172 eration caused by the central term (GRAV μ/r ; 8.5 m s^{-2}) is projected mainly
173 in the radial direction because of the almost circular orbit of the GRACE satel-
174 lites. Then follows the acceleration due to the Earth flattening (GRAV J_2) and to
175 the remaining terms of the geopotential (GRAV rest). Considering the range of
176 the nongravitational accelerations (DRAG, DSRP, ALB, IR: $1\text{--}500 \text{ nm s}^{-2}$), it is
177 clear that for a successful accelerometer calibration also the other accelerations
178 of gravitational origin must be taken into account: direct lunisolar perturbations
179 (LUNISOL), solid Earth tides (SETID), ocean tides (OTID), and relativistic cor-

180 rection (REL).

181 2.4. Geopotential – acceleration with respect to its degree

182 The graphs in Figure B.4 show the accelerations produced by the spherical
183 harmonic terms of the geopotential model EGM96 summed over the orders for a
184 given degree. The individual curves correspond to the altitude of a satellite in a
185 circular orbit around the Earth.

186 The histograms in Figure B.3 set the upper limit of the nongravitational ac-
187 celerations acting on the GRACE satellites to be 500/30/70 nm s^{-2} for the along-
188 track/cross-track/radial components, while the altitude of the satellites decreased
189 from 510 km to 450 km. From Figure B.4 we infer that the geopotential-induced
190 accelerations approximately equal in magnitude to the upper limit must start at de-
191 gree 50–60/80–100/70–90 and go up to degree 125–150 to cover 1 nm s^{-2} lower
192 limit of the nongravitational acceleration level, or up to degree 150–180 to reach
193 0.1 nm s^{-2} . In this study, we used the geopotential harmonic expansion up to
194 degree and order 180 (or the maximum allowable value of a given model).

195 Figure 4 should be positioned here.

196 3. Method of calibration – a general look

197 In this section, we will explain the proposed method of calibration using the
198 simulated positions and accelerations. To the simulated satellite positions we will
199 add white noise of a known variance, to have an approximate representation of
200 the POD positions. The uncalibrated accelerometer data will be represented by

201 the simulated nongravitational accelerations, shifted and scaled by given values.
202 We will look for a linear filter that would realize the second derivative of positions,
203 taking into account the character of the waveforms in question (Figs. B.1 and B.2).
204 Filtering the positions yields the estimated second derivatives, the POD-based to-
205 tal acceleration vectors, from which the modelled gravitational accelerations are
206 subtracted. In this way, the POD-based nongravitational acceleration vector is
207 obtained, which serves as the calibration standard (etalon). The calibration equa-
208 tion then connects the mean curve, given here by the simulated nongravitational
209 accelerations, with the calibration standard as the observation vector containing a
210 random component. From this simple linear regression model, we find the bias
211 and scale factor as the calibration parameters for each accelerometer component.
212 When filtering the positions, the filter of the second derivative introduces serial
213 correlation into the random component of the POD-based nongravitational accel-
214 erations. While the mean values of the fitted calibration parameters are not much
215 affected, the standard fit error and all the confidence intervals are not correct. The
216 generalized least squares method (GLS) is used to find the correct estimates of the
217 uncertainty in the calibrated nongravitational accelerations.

218 An important aspect of the presented calibration method is that we use the
219 kinematic orbits, i.e. those determined directly from GPS measurements and not
220 influenced by any force models (cf. Ditmar et al., 2006). This is of concern es-
221 pecially for modelling the accelerations due to the geopotential, where different
222 geopotential models might give different POD-based nongravitational signals. It is
223 an assumption of the presented method that the noise in the modelled gravitational
224 accelerations is negligible compared to that of the POD-based total acceleration
225 (more on this point in Sec. 5.4).

226 *3.1. Simulated POD positions*

227 Simulated positions are computed by the numerical integration of the satellite
 228 motion using the simulated gravitational $\mathbf{a}_{\text{GRAV}}^{\text{SIM}}$ and nongravitational $\mathbf{a}_{\text{NG}}^{\text{SIM}}$ accel-
 229 erations (SIM stands for ‘simulated’ or ‘modelled’). The time step of positions
 230 and other quantities used in this study is 10 seconds. To these approximately
 231 error-free positions, which are given in the celestial reference frame, we added a
 232 normally distributed white noise Z , with a variance of $\sigma^2=1$ cm in each position
 233 component. The resulting sequence of random vectors \mathbf{r} represents the kinematic
 234 positions from the POD.

235 *3.2. Filter of the second derivative*

236 We obtain the POD-based total accelerations $\mathbf{a}_{\text{TOTAL}}^{\text{POD}}$ by double differentiation
 237 of the positions \mathbf{r} . For this purpose we used the *Savitzky-Golay* or *polynomial*
 238 *smoothing filters* (e.g., Press et al., 2001). A polynomial of a chosen order is
 239 least-squares fitted to the data points within a running window of a chosen length;
 240 the approximate numerical derivative at the central point is obtained by the differ-
 241 entiation of the fitted polynomial.

242 We looked for the best agreement between the simulated and POD-based non-
 243 gravitational accelerations, when no noise in positions is introduced. We started
 244 with the first approximation to the numerical second derivative, the simple three-
 245 -point formula, but we found that such low order derivatives produce too high a
 246 bias (10^{-6} m s $^{-2}$ with the time step of 1 sec, 10^{-4} m s $^{-2}$ with 10 sec) between the
 247 simulated and POD-based nongravitational accelerations. We then systematically
 248 tested many combinations of the polynomial orders and window lengths to find a
 249 suitable pair with low values of both parameters that would produce a satisfactory
 250 agreement between the simulated and POD-based nongravitational accelerations.

251 Finally, we have chosen the combination of the polynomial order 6 with the win-
 252 dow length 9; other combinations, e.g. 8/13, 9/11, 9/21 yielded similar results.
 253 The tested combinations comprised also the case with no smoothing, where the
 254 window length equals the polynomial order plus one, but again, the bias was too
 255 high for our purposes. For later reference, we will symbolically write the filtering
 256 of positions as the convolution of the second-derivative filter \mathcal{F} and the radius-
 257 vector \mathbf{r} ,

$$\mathbf{a}_{\text{TOTAL}}^{\text{POD}} = \mathcal{F} * \mathbf{r}. \quad (1)$$

258 3.3. POD-based nongravitational accelerations

259 The calibration standard, the POD-based nongravitational acceleration vec-
 260 tor $\mathbf{a}_{\text{NG}}^{\text{POD}}$, is obtained from the POD-based vector of total accelerations $\mathbf{a}_{\text{TOTAL}}^{\text{POD}}$ by
 261 subtracting the modelled accelerations of gravitational origin $\mathbf{a}_{\text{GRAV}}^{\text{SIM}}$,

$$\mathbf{a}_{\text{NG}}^{\text{POD}} = \mathbf{a}_{\text{TOTAL}}^{\text{POD}} - \mathbf{a}_{\text{GRAV}}^{\text{SIM}}, \quad (2)$$

262 where the vector $\mathbf{a}_{\text{GRAV}}^{\text{SIM}}$ is the sum of the acceleration vectors caused by the Earth
 263 static gravitational field, direct lunisolar perturbations, solid Earth and ocean tides,
 264 and relativistic effects (Sec. 2.3). The relatively high degree and order of the
 265 geopotential model, which is necessary for the generation of gravitational accel-
 266 erations of low enough magnitude comparable to that of the calibrated accelerom-
 267 eter measurements, was discussed in Section 2.4.

268 While the numerical differentiation of the positions is most easily done in the
 269 (inertial) celestial reference frame, the POD-based nongravitational accelerations
 270 obtained in Eq. (2) must be projected into the science reference frame, in which
 271 all GRACE Level-1B data products are specified (Case et al., 2004). The axes
 272 of the science reference frame are close to those of the satellite local reference

273 frame (Sec. 2.2) to within a few degrees, except for the sign. In this section,
 274 we use the exact satellite local reference frame, in Section 4, where the attitude
 275 information of the GRACE satellites is used, we perform a simple sign change
 276 to have all our calculations and figures in an approximate satellite local reference
 277 frame. The motivation for using the satellite local reference frame lies in its clear
 278 physical meaning, e.g. the air drag vector always points in the negative along-
 279 track direction, the terrestrial infrared radiation in the positive radial direction.

280 In Figure B.5 the components of the POD-based nongravitational acceleration
 281 vector $\mathbf{a}_{\text{NG}}^{\text{POD}}$ in the satellite local reference frame are shown. Using the second-
 282 derivative filter, the 1-cm noise in positions is amplified to high-frequency noise
 283 in accelerations with oscillations on the order of 10^{-4} m s^{-2} . The “true” signal
 284 $\mathbf{a}_{\text{NG}}^{\text{SIM}}$ of amplitudes 10–500 nm s^{-2} is buried in noise.

285 Figure 5 should be positioned here.

286 3.4. Calibration equation

287 The calibration equation is given by the linear model

$$288 \mathbf{a}_{\text{NG}}^{\text{POD}} = \mathbf{B} + S \mathbf{a}_{\text{ACC}}^{\text{UNCAL}} + \boldsymbol{\epsilon}, \quad (3)$$

288 where \mathbf{B} is bias, S scale factor, $\mathbf{a}_{\text{ACC}}^{\text{UNCAL}}$ uncalibrated accelerometer data, $\boldsymbol{\epsilon}$ statisti-
 289 cal error. On the assumption that the accelerometer measures independently in its
 290 three axes, we have one independent calibration equation (3) for each accelerom-
 291 eter axis.

292 In this section, the uncalibrated data $\mathbf{a}_{\text{ACC}}^{\text{UNCAL}}$ are represented by the simulated

293 nongravitational accelerations $\mathbf{a}_{\text{NG}}^{\text{SIM}}$, which were scaled by $S=1.1$ and shifted by
 294 $B=1.2\times 10^{-6}\text{m s}^{-2}$.

295 3.5. Problem of autocorrelated noise

296 The probability model, $y = b_0 + b_1x + \epsilon$, for which the ordinary least squares
 297 (OLS) method of estimation is best suited, relates the error-free predictor variable
 298 x and the random variable y (see Appendix A). In this respect, the calibration
 299 equation (3) matches well the OLS model: the noise in the simulated nongravita-
 300 tional accelerations $\mathbf{a}_{\text{NG}}^{\text{SIM}} \equiv x$ is several orders of magnitude lower than that of the
 301 response variable $\mathbf{a}_{\text{NG}}^{\text{POD}} \equiv y$ (Fig. B.5). Also the noise in the accelerometer readouts
 302 should be, according to the specifications (Sec. 2.1), much lower than that of $\mathbf{a}_{\text{NG}}^{\text{POD}}$.

303 The OLS provide correct uncertainty estimates, if the errors ϵ are independent
 304 and normally distributed. If the random errors are positively correlated, the uncer-
 305 tainty in the fitted parameters is usually underestimated, thus giving a false sense
 306 of accuracy (e.g., Chatterjee and Hadi, 2006; Rawlings et al., 1998).

307 When a digital filter is applied to a data sequence containing a random compo-
 308 nent, the random errors within the filter window are linearly combined to the new
 309 output value; hence the newly formed random vector has components, which are
 310 correlated. This happens to the POD-based nongravitational accelerations $\mathbf{a}_{\text{NG}}^{\text{POD}}$
 311 obtained from the positions by applying the second-derivative filter (1) and after
 312 subtracting the modelled accelerations of gravitational origin in Eq. (2); the noise
 313 in positions, which in this section is supposed to be white (Sec. 3.1), after filtering
 314 becomes a correlated random component of $\mathbf{a}_{\text{NG}}^{\text{POD}}$. The OLS applied to the calibra-
 315 tion equation (3) now enables one to calculate acceptable estimates of B and S , as
 316 the point estimates of the regression parameters are usually not much affected by
 317 the autocorrelated errors, but it is not possible to correctly estimate the uncertainty

318 of the calibrated accelerations. For a correct estimation of the uncertainties in B
 319 and S , we will use the generalized least squares method; see Appendix B for a
 320 short review.

321 3.6. Use of GLS to remove autocorrelation

322 In fact, the non-diagonal covariance matrix of the random component in $\mathbf{a}_{\text{NG}}^{\text{POD}}$
 323 was created by the action of the second-derivative filter \mathcal{F} from the covariance
 324 matrix of the white noise $\text{Var}(Z_i) = \sigma^2 \mathbf{1}$. Namely,

$$\text{Var}(\epsilon) = F \text{Var}(Z) F' = \sigma^2 F F', \quad (4)$$

325 where F is a square matrix, generated from the coefficients of the filter \mathcal{F} and
 326 whose multiplication is equivalent to the action of the filter (e.g., Gray, 2006).
 327 But the situation, where we *know* the covariance matrix of the random errors in a
 328 linear model, is exactly what the GLS method is suited for. In our case, finding the
 329 GLS transformation matrix is straightforward, $W = F^{-1}$. After applying W to the
 330 calibration equation (3), and solving the transformed equation (Eq. B.3) through
 331 the OLS, the residuals become again uncorrelated and the original σ^2 should be
 332 recovered. As regards the implementation of the filtering, we throw away the first
 333 and last few acceleration points during the filter warm-up phase, and we find the
 334 transformation matrix W through the Cholesky decomposition of the covariance
 335 matrix $F F'$ (cf. Eq. B.2).

336 3.7. Decorrelation of the observations

337 The results of the GLS transformation of the POD-based nongravitational ac-
 338 celerations $\mathbf{a}_{\text{NG}}^{\text{POD}}$ are in Figure B.6; only the solution in the along-track compo-
 339 nent is shown. As the GLS transformation matrix $W = F^{-1}$ is actually the inverse

340 to the second-derivative filter, which produces accelerations from positions, the
 341 “nongravitational positions” are obtained as a sort of double integral of $a_{\text{NG}}^{\text{POD}}$. Ef-
 342 fectively, we got back into the positions, but now with the gravitational signal
 343 removed.

344 In the upper panel of Figure B.6, the nongravitational positions are shown
 345 (y_{OLS1}) as the observations for the OLS estimates, and the fitted function (\hat{y}_{OLS1}),
 346 which is the simulated nongravitational acceleration $a_{\text{NG}}^{\text{SIM}}$ transformed to positions
 347 by W . Several statistics shown in the lower panels confirm the fact that the OLS
 348 residuals in the middle panel are uncorrelated normal: autocorrelation function
 349 (ACF), partial autocorrelation function (PACF; more about it in Sec. 4.2), normal
 350 probability plot and Jarque-Bera test (e.g., Brockwell and Davis, 2002). Through
 351 the OLS applied to the transformed linear model (Eq. B.3), apart from the es-
 352 timates of the calibration parameters \hat{b}_0 and \hat{b}_1 , the original error variance of the
 353 nongravitational positions (Sec. 3.1) is estimated by the OLS residual mean square
 354 $\hat{\sigma}^2$ (labelled as $\sigma_{\text{iid,est}}$ in Fig. B.6).

355 Figure 6 should be positioned here.

356 3.8. *Very high correlation between the calibration parameters*

357 In Figure B.6 the reader may have noticed that the coefficient of correlation
 358 between the fitted calibration parameters \hat{b}_0 and \hat{b}_1 is very close to one, typically,
 359 when calibrating the simulated or real accelerometer data, we get $\rho(\hat{b}_0, \hat{b}_1) \approx 0.999$. . .
 360 Of course, such a high correlation is not good for the stability of the fitted param-
 361 eters. The cause of this situation lies in the collinearity of the predictor variables,

362 one of the standard problems encountered in multiple regression (e.g., Chatterjee
363 and Hadi, 2006; Rawlings et al., 1998; Weisberg, 2005).

364 For simplicity, let us use for the calibration equation (3) the notation of the
365 OLS from Appendix A and calibrate the accelerometer measurements against
366 the simulated nongravitational accelerations, so in this subsection $x \equiv \mathbf{a}_{\text{ACC}}^{\text{UNCAL}}$ and
367 $y \equiv \mathbf{a}_{\text{NG}}^{\text{SIM}}$. We may approximately take both x (Fig. B.2) and y (Fig. B.1) as signals
368 made up by two components, by a constant signal plus an oscillatory component
369 (sum of sinusoids). This is not very far from the truth, as the patterns of one
370 revolution in Figures B.1 and B.2 repeat themselves relatively regularly during a
371 period of weeks or so. From the point of view of Fourier analysis, the constant
372 component \bar{x} and the oscillatory component $(x - \bar{x})$ are orthogonal to each other,
373 the same applies to \bar{y} and $(y - \bar{y})$, so comparing the constants \bar{x} , \bar{y} would produce
374 an estimate of an ‘intuitive’ bias, i.e. a distance between the mean values \bar{x} and
375 \bar{y} , and fitting the oscillations $(x - \bar{x})$ and $(y - \bar{y})$ would estimate the ‘scale factor’,
376 i.e. a mean ratio of the oscillatory amplitudes (provided that x and y are in phase,
377 which is true here). But this is not the case of the calibration equation (3); here
378 the parameter b_1 multiplies the predictor x , which is a sum of the constant \bar{x} and
379 oscillations $(x - \bar{x})$, but the predictor connected with b_0 is also a constant, hence
380 the collinearity. What makes the correlation between \hat{b}_0 and \hat{b}_1 so high is the very
381 large value of the offset \bar{x} in the accelerometer readouts compared to the ampli-
382 tude of the oscillations $(x - \bar{x})$. For large sample sizes and $\bar{x}^2 \gg \hat{\sigma}_x^2$, where $\hat{\sigma}_x^2$ is
383 the sample variance of x , we may approximate the expression for the coefficient
384 of correlation (Eq. A.6) by

$$\rho(\hat{b}_0, \hat{b}_1) = \frac{-\bar{x}}{\sqrt{\hat{\sigma}_x^2 + \bar{x}^2}} \simeq \frac{-\bar{x}}{|\bar{x}|} \left(1 - \frac{1}{2} \frac{\hat{\sigma}_x^2}{\bar{x}^2} \right). \quad (5)$$

385 Taking the along-track component of $\mathbf{a}_{\text{ACC}}^{\text{UNCAL}}$ in Figure B.2 as a quantitative ex-

386 ample, the power of the constant component $\bar{x}^2 \simeq (10^{-6})^2 \text{ m}^2 \text{ s}^{-4}$ and that of the
 387 oscillatory component $\hat{\sigma}_x^2 \simeq (5 \cdot 10^{-8})^2 / 2 \text{ m}^2 \text{ s}^{-4}$ give $\rho(\hat{b}_0, \hat{b}_1) \simeq 0.9995$.

388 The extremely high correlation between the parameters \hat{b}_0 and \hat{b}_1 may be
 389 avoided by changing the calibration model (3). From Eq. (5), the correlation be-
 390 tween the parameters in the simple linear regression is zero, if the predictor x has
 391 zero mean. In the notation of Appendix A, a modified calibration model might be

$$y - \bar{y} = b_0^* + b_1^*(x - \bar{x}) + \epsilon, \quad (6)$$

392 together with the definitions $y^* = y - \bar{y}$ and $x^* = x - \bar{x}$. The modified model has
 393 perfectly uncorrelated parameters b_0^* and b_1^* , moreover, one can easily show that
 394 $b_0^* = \bar{y} - \bar{x}$ is the ‘intuitive’ bias mentioned above. The scale factors b_1, b_1^* of both
 395 models have the same fitted value, $\hat{b}_1^* = \hat{b}_1$, and, perhaps surprisingly, also the same
 396 standard error, $\hat{\sigma}(\hat{b}_1) = \hat{\sigma}(\hat{b}_1^*)$. Only the modified intercept b_0^* has a substantially
 397 smaller standard error, from (A.4), $\hat{\sigma}(\hat{b}_0^*) = \hat{\sigma} / \sqrt{n}$. Indeed, the calculated values of
 398 the modified intercept \hat{b}_0^* are much less noisy compared to those of \hat{b}_0 . But on
 399 rearranging the terms in (6), $y = \bar{y} + b_0^* - b_1^* \bar{x} + b_1^* x + \epsilon$, one can express the ‘old’
 400 calibration parameters b_0 and b_1 by means of the modified ones,

$$b_0 = b_0^* + \bar{x}(1 - b_1^*), \quad b_1 = b_1^*. \quad (7)$$

401 We might believe that the ‘statistically better’, completely uncorrelated parame-
 402 ters b_0^*, b_1^* and their uncertainties would somehow help b_0, b_1 to have less correla-
 403 tion – but this does not happen; starting from (7) and using the rules for variances
 404 of the linear functions of random variables (e.g., Rawlings et al., 1998), we arrive
 405 at exactly the same formulae (A.4), (A.6) as before.

406 In this study, for the regression calculations themselves we used the modified
 407 model (6). During the inversion of the normal equations, MATLAB (2007) indi-

408 cated a bad condition number, which was caused by a difference of several orders
409 between the magnitudes of the two predictors; a simple solution was to multiply
410 the intercept b_0^* by 10^{-7} . In fact, both these computational modifications are anal-
411 ogous to standardizing the predictor variables in multiple regression or using the
412 MATLAB option ‘center and scale X data’. For the sake of comparison of our
413 calibration parameters with those computed by other groups, and because, after
414 all, the calibration models (3) and (6) are equivalent, the final results are given in
415 terms of the original parameters b_0 and b_1 .

416 **4. Calibration of the accelerometer data over several revolutions**

417 In this section we will apply the calibration method to the real GRACE data
418 covering several orbital revolutions in order to analyze the calibration results in
419 more detail. As the POD positions, we used the high-quality 10-second kinematic
420 orbits of the GRACE satellites, kindly provided by D. Švehla (TU Munich). The
421 orbits were computed using the zero-difference ionosphere-free phase measure-
422 ments, the 10-sec orbits are based on the interpolated 30-sec POD satellite clocks
423 (Švehla and Rothacher, 2005).

424 The simulated gravitational accelerations, needed for obtaining the POD-based
425 nongravitational accelerations (Sec. 3.3), the coordinate transformations and the
426 simulated nongravitational accelerations were calculated by our own orbital prop-
427 agator NUMINTSAT (Bezděk et al., 2009). When working with the real-world
428 data, it has become clear that in contrast to simulations the use of the most up-to-
429 date physical models is crucial for obtaining meaningful calibration results. We
430 used: coordinate transformations between ICRF and ITRF systems (McCarthy
431 and Petit, 2003), the model of static gravitational field EIGEN-5C to order and

432 degree 180 (Förste et al., 2008), lunar and solar ephemerides JPL DE405, the
 433 model of solid Earth tides (anelastic Earth; McCarthy, 1996), the model of ocean
 434 tides CSR 4.0 (Bettadpur, 2004b).

435 We obtain the POD-based nongravitational accelerations $a_{\text{NG}}^{\text{POD}}$ in Eq. (2) using
 436 the second-derivative filter (1) and the modelled accelerations of gravitational ori-
 437 gin. Figure B.7 shows a typical result for the three accelerometer axes, the ampli-
 438 fied noise from the POD positions being roughly of the same order of magnitude
 439 as that for the simulated case in Figure B.5. The components shown in Figure B.7
 440 are not exactly ‘along-track’, ‘cross-track’ and ‘radial’, as the accelerometer read-
 441 outs are now given in the science reference frame (Sec. 3.3).

442 Figure 7 should be positioned here.

443 4.1. Correlated noise in the POD positions

444 We apply the GLS transform W to the calibration equation (3), which now
 445 relates the observations given by $a_{\text{NG}}^{\text{POD}}$ and the regressor equal to the uncalibrated
 446 accelerometer readouts $a_{\text{ACC}}^{\text{UNCAL}}$. The acquired “nongravitational positions” are in
 447 Figure B.8; clearly, the OLS residuals from the real POD positions are correlated
 448 (middle panel), which is confirmed by the graph of the estimated autocorrelation
 449 function (ACF; in blue, bottom left panel). This is not surprising, the kinematic
 450 orbits are reported to be correlated (Švehla and Földvary, 2006). On the other
 451 hand, the standard error of the OLS fit $\hat{\sigma}$ of a few centimetres as an estimate of
 452 the noise in the real kinematic POD positions is a plausible value.

453 Figure 8 should be positioned here.

454 4.2. Removing the autocorrelation with an AR model

455 In this subsection, we will use a general approach for drawing statistical in-
456 ferences from time series (Brockwell and Davis, 2002; Chatfield, 1995). In most
457 practical problems involving time series we see only one realization, but we imag-
458 ine it to be one of the many sequences that might have occurred. It is necessary
459 to setup a hypothetical probability model to represent the data; after an appropri-
460 ate family of models has been chosen, it is then possible to estimate parameters,
461 check for goodness of fit to the data, and possibly to use the fitted model.

462 We suppose that the correlated OLS residuals (middle panel of Fig. B.8) are a
463 realization of a stationary process and we want to represent its correlation structure
464 by fitting an appropriate autoregressive moving-average (ARMA) model. This
465 class of linear time series models has the property that any autocovariance func-
466 tion that asymptotically tends to zero can be approximated arbitrarily well by the
467 autocovariance function of some ARMA process. The fact that the sample au-
468 tocorrelation function (ACF) is negligible for some finite lag q suggests that a
469 moving-average model $MA(q)$ might provide a good representation of the data.
470 Analogously, the *partial autocorrelation function* (PACF; in cyan, bottom left
471 panel of Fig. B.8) of a causal autoregressive process $AR(p)$ is zero for lags greater
472 than p . Both the ACF and PACF of the OLS residuals are in the bottom left panel
473 of Figure B.8. The sample PACF clearly falling off, we chose the pure $AR(7)$
474 process to be fitted to the residuals using the Yule-Walker estimation. The ACF
475 of the fitted AR process of order 7 (in green, bottom left panel of Fig. B.8) agrees

476 well with the sample ACF for lags less than 100; in our experience, the order 7 is
 477 sufficient to match the correlation structure of the OLS residuals.

478 We suppose that the OLS residuals may be viewed as a realization of the fitted
 479 AR(7) process, in other words, as an output to filtering a white noise input by
 480 the corresponding AR filter. Therefore, the covariance matrix of the correlated
 481 residuals in Fig. B.8 is now given as that of the fitted AR process. This new
 482 covariance matrix replaces the matrix $Var(Z)$ in Eq. (4) and the GLS method
 483 is applied in the same way as in Section 3.6. We will use the subscript 2 to
 484 distinguish the new GLS transformation. The GLS_2 transformation matrix W_2
 485 is obtained numerically by the Cholesky decomposition of the new covariance
 486 matrix (Eq. B.2). After transforming the calibration equation (3) using W_2 , and
 487 using the OLS_2 estimation to find the calibration parameters, we finally obtain an
 488 approximately uncorrelated series of residuals, in the middle panel of Figure B.9.
 489 Indeed, the ACF and PACF (bottom left panel) are negligible except at zero lag.

490 Figure 9 should be positioned here.

491 4.3. Calibrated accelerometer measurements

492 On solving the calibration equation (3) by the GLS_2 method described in the
 493 previous section, we obtained the calibrated accelerometer measurements a_{ACC}^{CAL}
 494 and their estimated uncertainty band $\hat{\sigma}(a_{ACC}^{CAL})$ given by the confidence interval (B.5).
 495 The fact that the GLS_2 residuals appear to be approximately uncorrelated and nor-
 496 mal (bottom panels of Fig. B.9) for the along-track component permits us to use
 497 statistical inference and to assert that the ‘true’ signal measured by the accelerom-

498 eter should be located with a high level of confidence within the $\pm 3\hat{\sigma}(a_{\text{ACC}}^{\text{CAL}})$ band
 499 around $a_{\text{ACC}}^{\text{CAL}}$. This is in accordance with the usual definition of the *99.7-percent con-*
 500 *fidence interval*, within which we expect the ‘true’ value of the estimated param-
 501 eter to be located with the coverage probability of 99.7 %, when the normal dis-
 502 tribution is sampled (‘three-sigma rule’). For the statement of uncertainties in this
 503 study, we used the coverage factor (CF) of 1 (‘one-sigma’ uncertainty, coverage
 504 probability 68.3 %) or that of 3 (coverage probability 99.7 %).

505 The calibrated accelerometer measurements $a_{\text{ACC}}^{\text{CAL}}$ together with the $3\hat{\sigma}(a_{\text{ACC}}^{\text{CAL}})$
 506 uncertainty band for two orbital revolutions are in Figure B.10. The uncertainty
 507 band is wider when the fitted value is farther from the mean, similarly to the usual
 508 OLS model (A.7). The sample mean $\langle 3\hat{\sigma}(a_{\text{ACC}}^{\text{CAL}}) \rangle$, which we can use to characterize
 509 the obtained uncertainty band in the along-track component, is around 25 nm s^{-2} .

510 In the same way, we can use the calibration equation to fit the simulated non-
 511 gravitational accelerations and obtain $a_{\text{NG}}^{\text{SIM,CAL}}$. As is apparent from Figure B.10,
 512 the uncertainty bands of both $\hat{\sigma}(a_{\text{ACC}}^{\text{CAL}})$ and $\hat{\sigma}(a_{\text{NG}}^{\text{SIM,CAL}})$ are of similar size. But the
 513 calibration equation (3) was used in a usual OLS sense, however, after the GLS_2
 514 transformation W_2 was applied. In the bottom panel of Figure B.10 there are the
 515 calibrated accelerometer and simulated nongravitational accelerations with their
 516 means subtracted and then projected to the W_2 space. It is evident that the W_2
 517 transformation matrix is an integrator, which, inversely to the second-derivative
 518 filter (1), effectively filters out the high frequencies from both $a_{\text{ACC}}^{\text{CAL}}$ and $a_{\text{NG}}^{\text{SIM,CAL}}$.
 519 Indeed, the estimated frequency response of the filter W_2 shows that only sinu-
 520 soids of periods longer than 30 minutes are retained. Although the accelerometer
 521 waveform give more details in the ‘acceleration domain’ than the modelled non-
 522 gravitational accelerations, the calibration in the GLS-induced nongravitational

523 positions effectively smoothes these differences out, and the final uncertainties
 524 $\langle \hat{\sigma}(a_{\text{ACC}}^{\text{CAL}}) \rangle$ and $\langle \hat{\sigma}(a_{\text{NG}}^{\text{SIM,CAL}}) \rangle$ are very close.

525 Figure 10 should be positioned here.

526 Similar calibration results have been obtained also for the radial component;
 527 the mean uncertainty $\langle \hat{\sigma}(a_{\text{ACC}}^{\text{CAL}}) \rangle$ is around three times larger, but the normality of
 528 the GLS₂ residuals is questionable. In the cross-track direction, we have not suc-
 529 ceeded to find a suitable AR process to decorrelate the GLS₁ calibration residuals.
 530 So, in the cross-track and radial directions, we found the calibration parameters
 531 \hat{b}_0 and \hat{b}_1 , but we are not able to calculate a reliable estimate of the uncertainty
 532 of $a_{\text{ACC}}^{\text{CAL}}$. From the point of view of the atmospheric density modelling, this is
 533 not a problem, by far the strongest signal from the atmospheric drag is in the
 534 along-track component and besides, the cross-track and radial components of the
 535 accelerometer readouts contain the disturbing signal from the attitude thrusters.

536 **5. Evolution of calibration parameters over 1.5 years**

537 The presented calibration method has been applied to the accelerometer data
 538 of both GRACE satellites within a period of 1.5 years (08/2002–03/2004), for
 539 which the 10-sec kinematic orbits were available to us. The following calibration
 540 scheme is based on the assumption that the calibration parameters vary slowly
 541 in time. As the accelerometer data as well the POD positions contain relatively
 542 frequent portions of outliers (cf. Flury et al., 2008), we used a running window
 543 covering several satellite revolutions, within which we calibrated the accelerome-
 544 ter readouts. From these calibration results we selected the non-overlapping seg-

545 ments with the best statistical properties. Simple long-term expressions for the
 546 calibration parameters may be obtained by fitting the linear (or quadratic) regres-
 547 sion models to the selected calibration results. The long-term statistical results
 548 are better suited for a comparison of different gravitational models and calibration
 549 algorithms than a few days studies, where chance may play a role.

550 5.1. Long-term values of the obtained uncertainties

551 In the regression analysis, the squared standard error of the fit $\hat{\sigma}^2$ (A.5) is an
 552 estimate of the constant variance of the observations, provided the assumptions of
 553 the OLS are met. As a factor, $\hat{\sigma}$ then enters the uncertainty estimates (A.4, A.7, A.8).

554 Although the correlated noise in the POD positions prevents the usual $3\text{-}\sigma$ in-
 555 terpretation of the OLS_1 residuals (in the middle panel of Fig. B.8), in physics
 556 and engineering this ‘RMS value’ $\hat{\sigma}$ is widely used to characterize the power of
 557 the residual signal. The upper panel of Figure B.11 shows the standard error of
 558 the fit $\hat{\sigma}_{OLS_1}$ for the 1.5-year period. The label OLS_1 refers to the case, where the
 559 GLS transformation is based only on the inverse second derivative filter $W=F^{-1}$,
 560 and thus the accelerations a_{ACC}^{UNCAL} and a_{NG}^{SIM} are ‘integrated’ to give the ‘nongrav-
 561 itational positions’ (Sec. 3.6). This is interesting, because on supposing that the
 562 modelled gravitational accelerations have negligible errors, $\hat{\sigma}_{OLS_1}$ then estimates
 563 the RMS value of the POD positions when compared with the independently mea-
 564 sured accelerometer data. The figure shows that the empirical distributions of
 565 $\hat{\sigma}_{OLS_1}$ for both a_{ACC}^{CAL} and $a_{NG}^{SIM,CAL}$ are very close, with no statistically significant
 566 difference, their mean values being equal to around 3 cm with an approximate
 567 uncertainty of 1–2 cm.

568 The aim of this paper is to obtain the calibrated accelerometer data together
 569 with a realistic error bar. As mentioned in Section 4.3, this can be achieved in

570 the along-track component only. The uncertainty estimates of the calibrated ac-
 571 celerometer and simulated nongravitational accelerations $\hat{\sigma}(a_{\text{ACC}}^{\text{CAL}})$ and $\hat{\sigma}(a_{\text{NG}}^{\text{SIM,CAL}})$
 572 in the lower panel of Figure B.11 are again statistically equivalent, the mean un-
 573 certainty being $8.5 \pm 3.0 \text{ nm s}^{-2}$. This is due to the severe smoothing, when the
 574 accelerations $a_{\text{ACC}}^{\text{CAL}}$ and $a_{\text{NG}}^{\text{SIM,CAL}}$ are calibrated against the POD positions, as ex-
 575 plained in Section 4.3.

576 Figure 11 should be positioned here.

577 The results in Figure B.11 come from the calibrating the accelerometer data
 578 within a running window of 2 revolutions. We processed the accelerometer data
 579 from both GRACE satellites using the window of 2–4 orbital revolutions. The
 580 long-term results for both satellites were statistically equivalent. The estimated
 581 RMS value $\hat{\sigma}_{\text{OLS1}}$ of the POD positions compared to the integrated accelerometer
 582 signal is: 3–4 cm in the along-track, 4–7 cm in the cross-track, and 6–12 cm
 583 in the radial components, the values are increasing with the length of the fitting
 584 window. At the same time, the mean uncertainty of the calibrated accelerometer
 585 measurements $\langle \hat{\sigma}(a_{\text{ACC}}^{\text{CAL}}) \rangle$ in the along-track component decreased from 8.5 nm s^{-2}
 586 to 6.5 nm s^{-2} .

587 Let us note here that we also calibrated the accelerometer data without a spe-
 588 cial treatment of the autocorrelation present in the POD residuals (Sec. 4.2). Then,
 589 in the along-track component we obtained the long-term mean of the uncertainty
 590 $\langle \hat{\sigma}(a_{\text{ACC}}^{\text{CAL}}) \rangle = 1.0 \text{ nm s}^{-2}$, which is approximately 7 times “better” than that stated
 591 above (window of 3-revs. used). This illustrates the overly optimistic accuracy
 592 estimates, when the autocorrelated errors are ignored in the linear regression prob-

593 lems (Sec. 3.5, Appendix B).

594 *5.2. Long-term evolution of scale factors and biases*

595 In the long term, the scale factor \hat{b}_1 of the accelerometer data is approxi-
596 mately constant (upper panel of Figure B.12), with the mean value near 1 for
597 both GRACE satellites, with the $3\text{-}\sigma$ uncertainty of a few percent. Using the fitted
598 value of \hat{b}_1 and Eq. (7), the biases \hat{b}_0 are obtained, which we can subsequently
599 fit with a straight line regression model to obtain simple long-term expressions
600 (lower panel of Fig. B.12), similarly to Bettadpur (2004a).

601 In Figure B.13, there are the results of the same procedure applied to the mod-
602 elled nongravitational accelerations. While the long-term statistical results of the
603 scale factor \hat{b}_1 are comparable for both accelerometer-based and simulated ac-
604 celerations, the biases are different: on average, the simulated nongravitational
605 accelerations are very close to the calibration standard $a_{\text{NG}}^{\text{POD}}$, the fitted mean value
606 of \hat{b}_0 is less than 0.01 nm s^{-2} ; but the variation in the straight-line model of the
607 bias is 3–8 times greater in the simulated accelerations than in the accelerometer-
608 based accelerations. In other words, the long-term accelerometer bias is more
609 stable with respect to the calibration standard than the bias of the simulated non-
610 gravitational accelerations. This may be attributed to the fluctuating errors in the
611 nongravitational acceleration models, which depend on the orbital conditions.

612 Figure 12 should be positioned here.

613 Figure 13 should be positioned here.

614 *5.3. Comparison with the calibration parameters from an independent study*

615 In a technical note, Bettadpur (2004a) states the constant scale factors and
616 simple linear (or quadratic) models of the changes in bias for each accelerometer
617 axis of the GRACE A/B satellites. These estimates were obtained in the GRACE
618 data processing for the precise orbit and gravity field determination, and their limit
619 of applicability is from the launch until 1 November 2003.

620 Considering the very high correlation between the fitted calibration parameters
621 (Sec. 3.8), we can set the scale factors \hat{b}_1 equal to the values specified in Bettadpur
622 (2004a) and expect that the biases will ‘adapt’ their values accordingly. Indeed,
623 in the three accelerometer axes of GRACE A, Figure B.14 shows a similar time
624 evolution of our biases and those from the report. In this case, the fixed values
625 of the scale factors were 0.961 (along-track), 0.98 (cross-track), 0.94 (radial). We
626 obtained similar results for GRACE B, Figure B.15, for the fixed scale factors
627 0.947 (along-track), 0.97 (cross-track), 0.92 (radial).

628 Figure 14 should be positioned here.

629 Figure 15 should be positioned here.

630 *5.4. Uncertainties for different gravity field models*

631 In Table B.1, there are the long-term means of the estimated RMS of noise
632 in the POD positions $\langle \hat{\sigma}_{OLS1} \rangle$ and of the uncertainty in the calibrated accelerom-
633 eter measurements $\langle \hat{\sigma}(a_{ACC}^{CAL}) \rangle$ obtained using selected models of the static gravity
634 field. We calculated the accelerations for degree/order 180 or less, according to
635 the definition of the model (indicated by superscripts).

636 In the first group, there are the most recent models based also on the data
637 from the GRACE mission: EIGEN-5C (Förste et al., 2008), EGM08 (Pavlis et
638 al., 2008), GGM03C/S (Tapley et al., 2007). These models provided the best re-
639 sults; the accelerometer calibration also does not indicate any statistical difference
640 between the results from the combination and satellite-only gravity field models
641 GGM03C and GGM03S.

642 The second group in Table B.1 are models computed using the CHAMP data,
643 but not those from GRACE: EIGEN-CHAMP03S (Reigber et al., 2005b), DEOS_CHAMP-
644 01C_70 (Ditmar et al., 2006). To test the influence of including the higher degree
645 terms of the static geopotential models on the proposed accelerometer calibration,
646 we also used the EIGEN-5C model limited to degree/order 70 (Sec. 2.4). From the
647 statistical point of view, the results of this group of models are equivalent to the
648 GRACE models. While there is no visible change in the results pertaining to the
649 along-track component, those of the cross-track and radial components display a
650 slight systematic decrease in the precision for the models with the maximum de-
651 gree/order 70, which might be attributed to the lower magnitude of the nongravi-
652 tational accelerations in these directions (Fig. B.3). So for a precise accelerometer
653 calibration it is better to include the higher degree/order gravity terms.

654 The results based on the pre-CHAMP gravity models EGM96 (Lemoine et al.,

655 1998) and GRIM5C (Gruber et al., 2000) are worse by a factor of about 4 in the
656 cross-track and radial components. Thus the proposed accelerometer calibration
657 provides an indirect evidence that the gravity missions CHAMP and GRACE have
658 appreciably contributed to improve the higher degree/order terms of the current
659 global static gravity field models.

660 Table 1 should be positioned here.

661 The main purpose of including this section was to show that the calibration
662 method does not depend upon a particular gravity model used, in other words
663 that it is plausible to suppose that the errors in the accelerations derived from the
664 gravity field model are negligible compared to those of the accelerations derived
665 from kinematic positions. This is clearly demonstrated by the long-term results in
666 Table 1, where the four most recent gravity models, derived by different groups
667 using different processing schemes, give statistically equivalent results in all three
668 accelerometer components. Besides, if nowadays the best available gravitational
669 model EGM08 goes up to degree/order 2159, and the new EIGEN or GGM mod-
670 els go up to degree/order 360, then we may expect that they are consistent in
671 predicting the geopotential functionals with a relatively low limit of degree/order
672 less than 150 and that they should generate rather close vectors of the gravitational
673 acceleration.

674 **6. Discussion**

675 As mentioned in Section 1, many scientific teams have calculated the cali-
676 bration coefficients of the GRACE accelerometers for periods of differing length,

677 from days to years. The question of the accuracy of the calibrated accelerometer
678 measurements, however, seems not to be discussed very much, as either the pri-
679 mary research objective in other studies is the gravity field modelling, or the com-
680 plexity of the calibration process prevents the uncertainty estimates from quanti-
681 fying, e.g. due to regularization.

682 Van den Ijssel and Visser (2007) estimated the nongravitational accelerations
683 for the CHAMP and GRACE A satellites as piecewise constant empirical accel-
684 erations via the reduced-dynamic POD approach. To obtain a solution, regular-
685 ization was necessary. Only the longer wavelengths were recovered, at best in
686 the along-track direction, with a bias in the cross-track direction. The authors
687 concluded that no meaningful solution could be obtained in the radial direction.

688 Van Helleputte et al. (2009) used the reduced-dynamic POD technique to de-
689 termine the calibration parameters of the CHAMP and GRACE A/B satellites over
690 a 5-year period. The method needs strong constraints to be set on the a priori bias
691 values in the cross-track and radial direction.

692 For the derivation of the satellite accelerations from kinematic positions, Reubelt
693 et al. (2006) used the second derivative of the Gregory-Newton interpolation scheme;
694 the explicitly stated coefficients of the 9-point filter are the same as those from the
695 second derivative of a 9-point polynomial filter of order 8 (i.e. with no smoothing,
696 cf. Sec. 3.2). The choice of this filter was driven by the aim of the study, which
697 was the determination of the gravity field parameters from 2 years of the CHAMP
698 kinematic orbits without a regularization to guarantee an unbiased solution.

699 There are several scientific groups, which used the fitted ARMA models when
700 solving the inverse problem of the gravity field determination, but with different
701 aims and details of implementation compared to our method. In the context of

702 processing the future GOCE gradiometer data, Schuh (2003) used the discrete
703 linear filters and the GLS method for handling the correlated measurements in the
704 frequency domain. The target was to obtain decorrelated observational equations
705 and to distribute the computational effort to a cluster of computers. A need to treat
706 the huge least-squares problems in the gravity field determination motivated Klees
707 et al. (2003) and Ditmar et al. (2007) to study how the coloured noise represented
708 by the ARMA processes might be used as a fast method to solve a Toeplitz system
709 of linear equations.

710 Ditmar et al. (2007) points out that the assumption about the stationarity of
711 the noise in the kinematic POD positions may not be realistic in many cases, due
712 to a quickly changing constellation of visible GPS satellites for a LEO satellite,
713 and therefore, the orbit accuracy may vary considerably in time. This might be
714 the reason for the increase in the estimated RMS of the POD positions with longer
715 length of the fitting windows (Sec. 5.1).

716 The fact that the RMS of noise in the cross-track and radial components of
717 the POD positions is several times worse, when comparing the accelerometer cal-
718 ibration statistics based on the pre-CHAMP gravity field models with those using
719 the recent models including the CHAMP and GRACE data (Sec. 5.4), is in accor-
720 dance with a similar improvement in the accuracy of the radial orbit component
721 of the altimeter satellites (Klokočník et al., 2005, 2008).

722 **7. Conclusions**

723 In this study it was demonstrated that the proposed method of calibration
724 of the linear accelerometer measurements is capable of finding the point esti-
725 mates of the calibration parameters in all three accelerometer components for

726 both GRACE A/B satellites. A statistically correct estimate of the accuracy of
727 the calibrated accelerometer measurements have been obtained for the along-track
728 component of the accelerometer data.

729 The calibration procedure makes use of the generalized least squares method,
730 which might be useful in other linear regression problems, where one has to deal
731 with the correlated residuals. In the case of the accelerometer calibration, the sit-
732 uation is particularly convenient for the application of the GLS method, as we
733 know exactly the regression mean function, equal to the uncalibrated accelerom-
734 eter measurements, and we need to shift it to the “right place” determined by the
735 calibration standard.

736 From the point of view of aeronomy and atmosphere research, the most im-
737 portant is the along-track component of the accelerometer data, where the signal
738 from the atmospheric drag is dominant; moreover, the cross-track and radial com-
739 ponents of the accelerometer data contain the relatively strong disturbing signal
740 due to the action of the attitude control thrusters.

741 Throughout the study, we have also used the modelled nongravitational ac-
742 celerations, whose waveform matches well that of the accelerometer readouts but
743 is generally smoother, and in the cross-track and radial components it does not
744 contain the spikes caused by the attitude thrusters. After the calibration of the
745 along-track component, the accelerometer data and the modelled nongravitational
746 accelerations have approximately the same mean uncertainty; this is due to the
747 fact that the GLS calibration effectively integrates the acceleration signal, so in
748 the calibration only the longer period waves are actually used. This is closely
749 connected with the fact that the calibration standard is calculated from the orbital
750 positions.

751 We applied the calibration method to the accelerometer data covering a 1.5-
752 year period in 2002–2004. Taking into account the previous experience, we sup-
753 posed that the calibration parameters, i.e. the scale factors and biases for each
754 accelerometer axis, evolve slowly in time. We used the running window of 2–4
755 orbital revolutions, within which we calibrated the accelerometer data and finally
756 selected the non-overlapping segments with the best statistical results. The time
757 evolution of the calibration parameters agrees well with that published in an inde-
758 pendent report.

759 On the assumption that the errors in the modelled accelerations of gravitational
760 origin are very small, the GLS calibration method defines a transformation of the
761 accelerometer data, which may be used to estimate the RMS of noise in the kine-
762 matic positions. Based on this comparison between the POD kinematic positions
763 with the independently measured accelerometer data set, we found plausible mean
764 values of (3–4; 4–7; 6–12) cm in the (along-track; cross-track; radial) directions.

765 We compared the long-term calibration results for several models of the Earth
766 static gravity field. The recent models EIGEN-5, EGM08 and GGM03, which are
767 based also on the data from the CHAMP and GRACE missions, gave statistically
768 equivalent results, the mean uncertainty in the along-track component of the cali-
769 brated accelerometer data being 6.5–8.5 nm s⁻² (one sigma). The same long-term
770 results were also obtained using the EIGEN-CHAMP03 model, which does not
771 contain the GRACE data. The estimated statistical errors produced using the pre-
772 CHAMP gravity models were several times worse in the cross-track and radial
773 components.

774 **8. Acknowledgements**

775 The author would like to thank Dražen Švehla from TU Munich for providing
 776 the GRACE kinematic orbits. The ISDC online data centre of the GFZ is acknowl-
 777 edged for the GRACE data products used in this study ([http://isdc.gfz-potsdam.de/
 778 grace/](http://isdc.gfz-potsdam.de/grace/)), the ICGEM centre of the IAG for the coefficients of the global gravity field
 779 models (<http://icgem.gfz-potsdam.de/ICGEM/>). Thanks are also due to Jaroslav
 780 Klokočník and Radek Peřestý for useful discussions, and to the reviewers for their
 781 relevant comments leading to many improvements in the manuscript.

782 **Appendix A. Ordinary least squares (OLS)**

783 In the *ordinary least squares* we suppose that the vector of observations y
 784 is given as the sum of a deterministic mean function $E(y)$ to which a vector of
 785 random errors ϵ with constant variance is added. The probability model of the
 786 *simple linear regression* is

$$y = b_0 + b_1x + \epsilon, \quad (\text{A.1})$$

787 where y is the vector of n observations, b_0 intercept, b_1 slope, x predictor, ϵ statis-
 788 tical error. The OLS estimates \hat{b}_0 and \hat{b}_1 are given by

$$\hat{b}_1 = SXY/SXX, \quad \hat{b}_0 = \bar{y} - \hat{b}_1\bar{x}, \quad (\text{A.2})$$

789 where $SXY = \sum (x_i - \bar{x})(y_i - \bar{y})$, $SXX = \sum (x_i - \bar{x})^2$. Using \hat{b}_0 and \hat{b}_1 we form the fitted
 790 function \hat{y} as the estimate of the mean function $E(y)$

$$\hat{y} = \hat{b}_0 + \hat{b}_1x. \quad (\text{A.3})$$

791 Under the assumption that the errors ϵ_i are independent and normal with constant
 792 variance σ^2 , the OLS estimates \hat{b}_0 , \hat{b}_1 are also normally distributed with the stan-

793 dard errors

$$\hat{\sigma}(\hat{b}_1) = \frac{\hat{\sigma}}{\sqrt{SXX}}, \quad \hat{\sigma}(\hat{b}_0) = \hat{\sigma} \sqrt{\frac{1}{n} + \frac{\bar{x}^2}{SXX}}, \quad (\text{A.4})$$

794 where the standard error of the OLS fit is

$$\hat{\sigma} = \sqrt{\sum_{i=1}^n (y_i - \hat{y})^2 / (n - 2)}. \quad (\text{A.5})$$

795 In general, the estimated parameters are correlated with the coefficient of correlation (Weisberg, 2005)

$$\rho(\hat{b}_0, \hat{b}_1) = \frac{-\bar{x}}{\sqrt{SXX/n + \bar{x}^2}}. \quad (\text{A.6})$$

797 We can calculate the uncertainty band around the fitted function \hat{y} , which is
798 called the *confidence interval*,

$$\hat{\sigma}(\hat{y}_i) = \hat{\sigma} \sqrt{\frac{1}{n} + \frac{(x_i - \bar{x})^2}{SXX}}, \quad (\text{A.7})$$

799 and the *prediction interval*, the uncertainty of a single (possibly future) observa-
800 tion y_F ,

$$\hat{\sigma}(y_F) = \hat{\sigma} \sqrt{1 + \frac{1}{n} + \frac{(x_F - \bar{x})^2}{SXX}}. \quad (\text{A.8})$$

801 **Appendix B. Generalized least squares (GLS)**

802 Defining X as the matrix of predictors and b as the vector of parameters, let

$$y = Xb + \epsilon \quad (\text{B.1})$$

803 be an OLS problem, where the post-fit tests showed that the random errors ϵ_i are
804 correlated or have a nonconstant variance, i.e. the covariance matrix of the random
805 errors is not equal to the scaled identity matrix, $\text{Var}(\epsilon) \equiv \sigma^2 V \neq \sigma^2 \mathbb{1}$. The *general-*
806 *ized least squares* (GLS) then define a linear transformation (e.g., Rawlings et al.,

807 1998)

$$W = T^{-1}, \quad \text{where} \quad V = TT', \quad (\text{B.2})$$

808 which maps the original linear model into a new one,

$$y^* = X^*b + \epsilon^*, \quad (\text{B.3})$$

809 such that the covariance matrix of the transformed errors ϵ^* is again a scaled identity matrix. Indeed,

$$\text{Var}(\epsilon^*) = W\text{Var}(\epsilon)W' = \sigma^2 T^{-1}TT'T^{-1'} = \sigma^2 \mathbf{1}. \quad (\text{B.4})$$

811 In the transformed variables, $y^*=Wy$, $X^*=WX$, the usual OLS are then used to
 812 find the regression parameters b of the *original* problem with correct estimates
 813 of their uncertainties. The thus obtained GLS estimator \hat{b} is also known as the
 814 Aitken estimator. By using the inverse transformation matrix $T=W^{-1}$, we may
 815 obtain the confidence and prediction intervals of the *original* fitted function $\hat{y}=T\hat{y}^*$
 816 from (A.7) and (A.8). Namely, the estimated confidence interval of \hat{y} is expressed
 817 in matrix notation as the square root of the diagonal of the covariance matrix

$$\text{Var}(\hat{y}) = \hat{\sigma}^2 TP^*T', \quad (\text{B.5})$$

818 where $P^* \equiv X^*(X^{*'}X^*)^{-1}X^{*'}$ is the ‘hat matrix’ of the transformed model.

819 Figure 16 should be positioned here.

820 Figure 17 should be positioned here.

821 To illustrate the importance of taking into account the autocorrelated errors,
822 we generated the random errors ϵ as a realization of an autoregressive model of
823 order 7 with coefficients found in Section 4.2. In Figure B.16 we directly used
824 the OLS to find \hat{y} as an estimate of the true value $E(y)=10$. The standardized
825 residuals and the estimated autocorrelation function of the residuals (middle and
826 bottom panels) show clearly that the residuals are correlated. The confidence
827 interval with the coverage factor of 3 locates the estimated true value within the
828 interval $\hat{y} \pm 3\hat{\sigma}(\hat{y}) = 9.02 \pm 0.21$; this interval is too narrow, it does not contain the
829 actual $E(y)$; using the OLS will not give correct uncertainty estimates.

830 When the GLS method is used to solve the problem with the same data (Fig. B.17),
831 the confidence interval of \hat{y} is 9.07 ± 3.8 and does indeed cover the true value. In
832 this example, the GLS confidence interval is approximately ten times larger than
833 that of the OLS estimate. Also the autocorrelation function of the OLS residuals
834 in the transformed variables, $y_i^* - \hat{y}_i^*$, is now that of a white noise (bottom panel of
835 Fig. B.17).

836 References

- 837 Aster, R. C., Borchers, B., Thurber, C. H., 2005. Parameter Estimation and Inverse Prob-
838 lems. Elsevier Academic Press.
- 839 Bettadpur, S., 2004a. Recommendation for a-priori bias & scale parameters for Level-1B
840 accelerometer data (Release 00). GRACE TN-04-02.
- 841 Bettadpur, S., 2004b. UTCSR Level-2 processing standards document. GRACE 327742,
842 Rev 1.1.
- 843 Bettadpur, S., 2007. Product Specification Document. GRACE 327-720, Rev 4.5.

- 844 Bezděk, A., Klokočník, J., Kostecký, J., Floberghagen, R., Gruber, C., 2009. Simulation
845 of free fall and resonances in the GOCE mission. *Journal of Geodynamics* 48, 47–53.
- 846 Brockwell, P. J., Davis, R. A., 2002. *Introduction to Time Series and Forecasting*.
847 Springer, 2nd ed., ISBN 0-387-95351-5.
- 848 Bruinsma, S., Thuillier, G., Barlier, F., 2003. The DTM-2000 empirical thermosphere
849 model with new data assimilation and constraints at lower boundary: accuracy and
850 properties. *Journal of Atmospheric and Solar-Terrestrial Physics* 65, 1053–1070.
- 851 Case, K., Kruizinga, G. L. H., Wu, S.-C., 2004. *GRACE Level 1B Data Product User*
852 *Handbook*. JPL, D-22027.
- 853 Chatfield, C., 1995. *The analysis of time series – An introduction*. Chapman & Hall/CRC,
854 5th ed., ISBN 9780412606304.
- 855 Chatterjee, S., Hadi, A. S., 2006. *Regression Analysis by Example*. Wiley/Interscience,
856 4th ed, ISBN 10 0-471-74696-7.
- 857 Ditmar, P., Kuznetsov, V., van der Sluijs, A. A. V. E., Schrama, E., Klees, R., 2006.
858 ‘DEOS_CHAMP-01C_70’: a model of the Earth’s gravity field computed from accel-
859 erations of the CHAMP satellite. *Journal of Geodesy* 79, 586–601.
- 860 Ditmar, P., Klees, R., Liu, X., 2007. Frequency-dependent data weighting in global gravity
861 field modeling from satellite data contaminated by non-stationary noise. *Journal of*
862 *Geodesy* 81, 81–96.
- 863 Doornbos, E., Förster, M., Fritsche, B., van Helleputte, T., van den IJssel, J., Koppenwall-
864 ner, G., Lühr, H., Rees, D., Visser, P., 2009. Air density models derived from multi-
865 satellite drag observations. ESA study, ESTEC contract 21022/07/NL/HE, DEOS/TU
866 Delft scientific report.
- 867 Flury, J., Rummel, R., Reigber, C., Rothacher, M., Boedecker, G., Schreiber, U. (Eds.),
868 2006. *Observation of the Earth System from Space*. Springer, ISBN 3-540-29520-8.
- 869 Flury, J., Bettadpur, S., Tapley, B. D., 2008. Precise accelerometry onboard the GRACE
870 gravity field satellite mission. *Advances in Space Research* 42, 1414–1423.

- 871 Förste, C., Flechtner, F., Schmidt, R., Stubenvoll, R., Rothacher, M., Kusche, J., Neu-
872 mayer, K.-H., Biancale, R., Lemoine, J.-M., Barthelmes, F., Bruinsma, J., Koenig, R.,
873 Meyer, U. 2008. EIGEN-GL05C – A new global combined high-resolution GRACE-
874 based gravity field model of the GFZ-GRGS cooperation. General Assembly EGU,
875 Vienna, Austria, Abstract No. EGU2008-A-06944.
- 876 Frommknecht, B., Fackler, U., Flury, J., 2006. Integrated Sensor Analysis GRACE. In:
877 Flury et al. (2006), 99–113.
- 878 Gray, R. M., 2006. Toeplitz and Circulant Matrices: A review. *Foundations and Trends in*
879 *Communications and Information Theory* 2(3), 155–239.
- 880 Gruber, T., Bode, A., Reigber, C., Schwintzer, P., Balmino, G., Biancale, R., Lemoine,
881 J.-M., 2000. GRIM5-C1: Combination solution of the global gravity field to degree
882 and order 120. *Geophysical Research Letters* 27, 4005–4008.
- 883 Klees, R., Ditmar, P., Broersen, P., 2003. How to handle colored observation noise in large
884 least-squares problems. *Journal of Geodesy* 76, 629–640.
- 885 Klokočník, J., Kostecký, J., Wagner, C. A., Schwintzer, P., Förste, C., Scharroo, R.,
886 2005. Evaluation of the accuracy of the EIGEN-1S and -2 CHAMP-derived gravity
887 field models by satellite crossover altimetry. *Journal of Geodesy* 78, 405–417.
- 888 Klokočník, J., Kostecký, J., Wagner, C. A., 2008. Improvement in the radial accuracy of
889 altimeter-satellite orbits due to the geopotential. *Earth Science Reviews* 91, 106–120.
- 890 Knocke, C., Ries, J. C., Tapley, B. D., 1988. Earth radiation pressure effects on satellites.
891 AIAA 88-4292, in *Proc. of the AIAA/AAS Astrodynamics Conference*, Minneapolis,
892 USA, 577–586.
- 893 Lemoine, F. G., Kenyon, S.C., Factor, J. K., Trimmer, R. G., Pavlis, N. K., Chinn, D. S.,
894 Cox, C. M., Klosko, S. M., Luthcke, S. B., Torrence, M. H., Wang, Y. M., Williamson,
895 R. G., Pavlis, E. C., Rapp, R. H., Olson, T. R., 1998. The Development of the Joint
896 NASA GSFC and the National Imagery and Mapping Agency (NIMA) Geopotential
897 Model EGM96. NASA/TP-1998-206861, GSFC.

- 898 MATLAB, 2007. Version 7.4.0.287 (R2007a), The MathWorks, Inc.
- 899 McCarthy, D. D., 1996. IERS Conventions (1996). IERS Tech. Note, No. 21, p. 1 - 95 21,
900 1–95.
- 901 McCarthy, D. D., Petit, G., 2003. IERS Conventions. IERS Technical Note 32,
902 <http://www.iers.org/iers/publications/tn/tn32/>.
- 903 Milani, A., Nobili, A. M., Farinella, P., 1987. Non-gravitational perturbations and satellite
904 geodesy. Adam Hilger, Bristol.
- 905 Montenbruck, O., Gill, E., 2001. Satellite Orbits – Models, methods and applications.
906 Springer, ISBN 3-540-67280-X.
- 907 Pavlis, N. K., Holmes, S. A., Kenyon, S. C., Factor, J. K., 2008. An Earth Gravitational
908 Model to Degree 2160: EGM2008. EGU, Vienna, Austria, April 13–18.
- 909 Press, W. H., Teukolsky, S. A., Vetterling, W. T., Flannery, B. P., 2001. Numerical recipes
910 in Fortran. Cambridge University Press, 2nd ed., ISBN 0 521 43064 X.
- 911 Rawlings, J. O., Pantula, S. G., Dickey, D. A., 1998. Applied Regression Analysis: A
912 Research Tool. Springer, 2nd ed., ISBN 0-387-98454-2.
- 913 Reubelt, T., Götzelmann, M., Grafarend, E. W., 2006. Harmonic analysis of the Earth's
914 gravitational field from kinematic CHAMP orbits based on numerically derived satel-
915 lite accelerations. In: Flury et al. (2006), 27–42.
- 916 Reigber, C., Lühr, H., Schwintzer, P. (Eds.), 2003: First CHAMP Mission Results for
917 Gravity, Magnetic and Atmospheric Studies, Springer, ISBN 3-540-00206-5.
- 918 Reigber, C., Lühr, H., Schwintzer, P., Wickert, J. (Eds.), 2005a. Earth Observation with
919 CHAMP. Results from Three Years in Orbit. Springer, ISBN 3540228047.
- 920 Reigber, C., Jochmann, H., Wunsch, J., Petrovic, S., Schwintzer, P., Barthelmes, F., Neu-
921 mayer, K.-H., König, R., Förste, C., Balmino, G., Biancale, R., Lemoine, J.-M., Loyer,
922 S., Perosanz, F., 2005b. Earth Gravity Field and Seasonal Variability from CHAMP. In:
923 Reigber et al. (2005a), 25–30.
- 924 Reigber, C., Lühr, H., Grunwaldt, L., Förste, C., König, R., Massmann, H., Falck, C.,

- 925 2006. CHAMP Mission 5 Years in Orbit. In: Flury et al. (2006), 3–7.
- 926 Schmidt, R., Flechtner, F., Meyer, U., Reigber, C., Barthelmes, F., Förste, C., Stubenvoll,
927 R., König, R., Neumayer, K.H., Zhu, S., 2006. Static and Time-Variable Gravity from
928 GRACE Mission Data. In: Flury et al. (2006), 115–129.
- 929 Schuh, W.-D., 2003. The Processing of Band-Limited Measurements; Filtering Tech-
930 niques in the Least Squares Context and in the Presence of Data Gaps. *Space Science*
931 *Reviews* 108, 67–78.
- 932 Švehla, D., Rothacher, M., 2005. Kinematic positioning of LEO and GPS satellites and
933 IGS stations on the ground. *Advances in Space Research* 36, 376–381.
- 934 Švehla, D., Földváry, L., 2006. From kinematic orbit determination to derivation of satel-
935 lite velocity and gravity field. In: Flury et al. (2006), 177–192.
- 936 Tapley, B., Reigber, Ch. (Eds.), 2002. GRACE Newsletter No. 1.
937 <http://podaac.jpl.nasa.gov/grace/>, <http://isdc.gfz-potsdam.de/grace/>.
- 938 Tapley, B. D., Bettadpur, S., Watkins, M., Reigber, C., 2004. The gravity recovery and
939 climate experiment: Mission overview and early results. *Geophys. Res. Lett.* 31, 9607–
940 9613.
- 941 Tapley, B., Ries, J., Bettadpur, S., Chambers, D., Cheng, M., Condi, F., Poole, S., 2007.
942 The GGM03 Mean Earth Gravity Model from GRACE. *Eos Trans. AGU* 88(52), Fall
943 Meet. Suppl., Abstract G42A-03.
- 944 Taylor, B. N., Kuyatt, C. E., 1994. Guidelines for Evaluating and Express-
945 ing the Uncertainty of NIST Measurement Results. NIST Technical Note 1297,
946 <http://physics.nist.gov/Pubs/guidelines/>.
- 947 van den Ijssel, J., Visser, P., 2007. Performance of GPS-based accelerometry: CHAMP
948 and GRACE. *Advances in Space Research* 39, 1597–1603.
- 949 van Helleputte, T., Doornbos, E., Visser, P., 2009. CHAMP and GRACE accelerometer
950 calibration by GPS-based orbit determination. *Advances in Space Research* 43, 1890–
951 1896.

952 Weisberg, S., 2005. Applied Linear Regression. Wiley/Interscience, 3rd ed., ISBN 0-471-
953 66379-4.

Accepted Manuscript

954

Figure captions

Figure B.1: Simulated nongravitational accelerations during one orbital revolution of the GRACE A satellite (11 Aug 2003). Shown are the components in the satellite local reference frame, namely the accelerations in the along-track (A-T; upper panel), cross-track (C-T; middle panel) and the radial direction (RAD; lower panel). The total acceleration (in black) is a superposition of the accelerations due to atmospheric drag (DRAG), direct solar radiation pressure (DSRP), reflected solar radiation pressure (ALB) and terrestrial infrared radiation (IR).

Figure B.2: Uncalibrated accelerometer data $\mathbf{a}_{\text{ACC}}^{\text{UNCAL}}$ (the same arc as in Fig. B.1).

Figure B.3: Histograms of gravitational and nongravitational accelerations in the satellite local reference frame components (GRACE A, 08/2002–03/2004).

Figure B.4: Acceleration due to the spherical harmonic terms of the gravitational model EGM96 grouped according to the degree.

Figure B.5: The POD-based nongravitational accelerations $\mathbf{a}_{\text{NG}}^{\text{POD}}$ in the satellite local reference frame (derived from the simulated POD positions). Also shown are the simulated nongravitational accelerations $\mathbf{a}_{\text{NG}}^{\text{SIM}}$.

Figure B.6: The ordinary least squares applied to “nongravitational positions”: observations and the fitted function (upper panel), residuals and numerical results of the fit (middle panel), several indicators that the residuals are uncorrelated and normal (lower panels). Simulated data were used, only along-track component is shown.

Figure B.7: The POD-based nongravitational accelerations $\mathbf{a}_{\text{NG}}^{\text{POD}}$ in the satellite local reference frame (derived from the kinematic positions, GRACE A, 25 Nov 2003).

Figure B.8: The ordinary least squares applied to “nongravitational positions” (panels as in Fig. B.6). Real data used (GRACE A, 25 Nov 2003, along-track).

Figure B.9: The ordinary least squares applied to the transformed residuals from Fig. B.8, the transformation matrix is based on the fitted AR(7) process.

Figure B.10: Calibrated accelerometer readouts and simulated nongravitational accelerations (upper panel), after centring and the transformation given by W_2 (bottom panel) (GRACE A, 25 Nov 2003, along-track).

Figure B.11: Time evolution of the standard fit error for the nongravitational positions (upper panels) and the uncertainty of the calibrated accelerations (lower panels) compared for the accelerometer-based and simulated nongravitational accelerations (GRACE A, along-track, window of 2 revs., approx. 2000 values).

Figure B.12: Long-term fit of the calibration parameters for the accelerometer measurements (GRACE A, along-track, window of 2 revolutions).

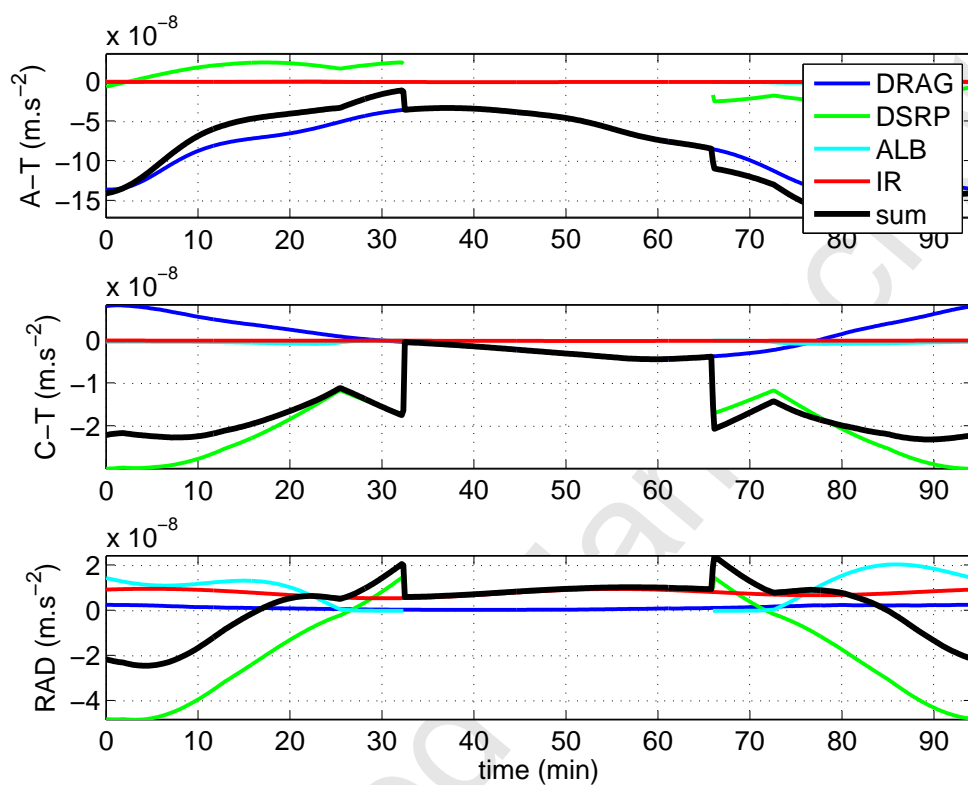
Figure B.13: Long-term fit of the calibration parameters for the simulated nongravitational accelerations (GRACE A, along-track, window of 2 revolutions).

Figure B.14: Comparison of the computed bias for GRACE A with that derived independently by Bettadpur (2004a).

Figure B.15: Comparison of the computed bias for GRACE B with that derived independently by Bettadpur (2004a).

Figure B.16: Example of a linear model with the errors generated by a stationary AR(7) process: the direct ordinary least squares solution. Upper panel: \hat{y}_{CI} define the confidence interval around \hat{y} , \hat{y}_{PI} the prediction interval; middle panel: standardized residuals and the fit results; lower panel: autocorrelation function of residuals.

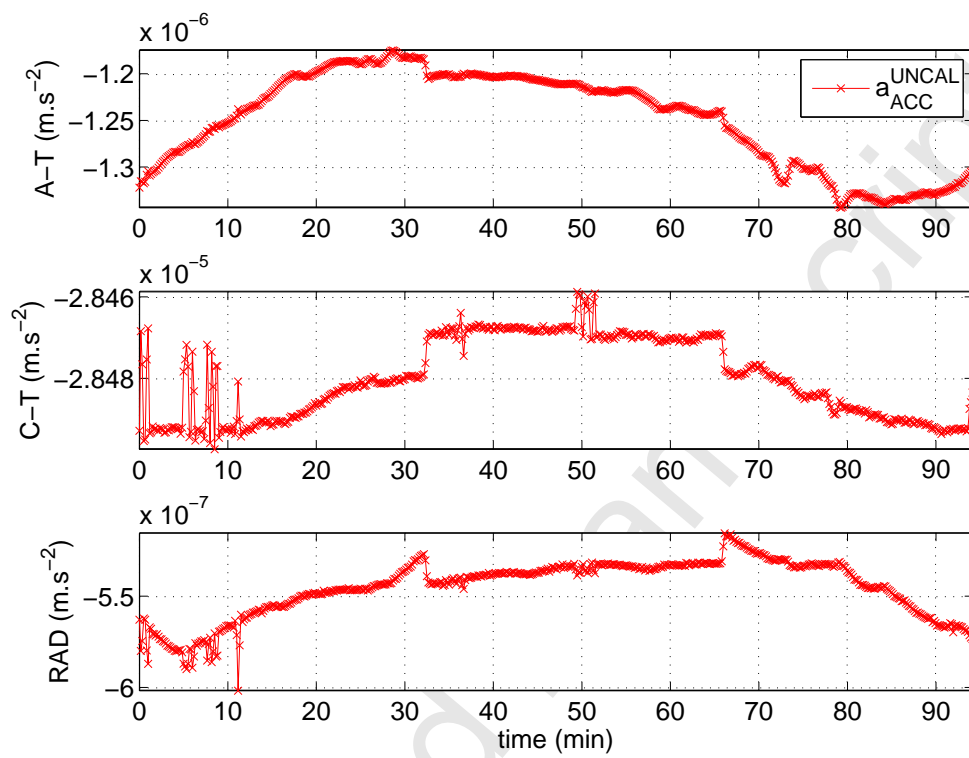
Figure B.17: Data as in Fig. B.16: the generalized least squares solution.



955

956

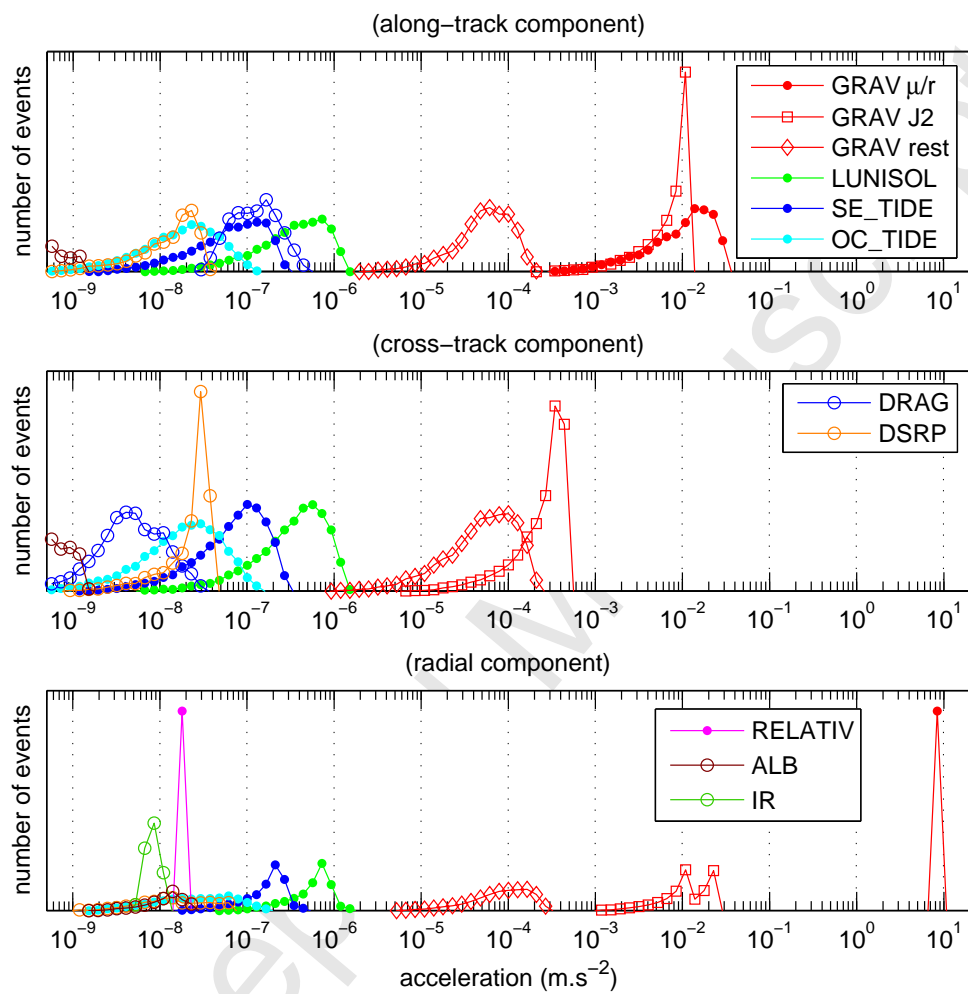
Figure 1



957

958

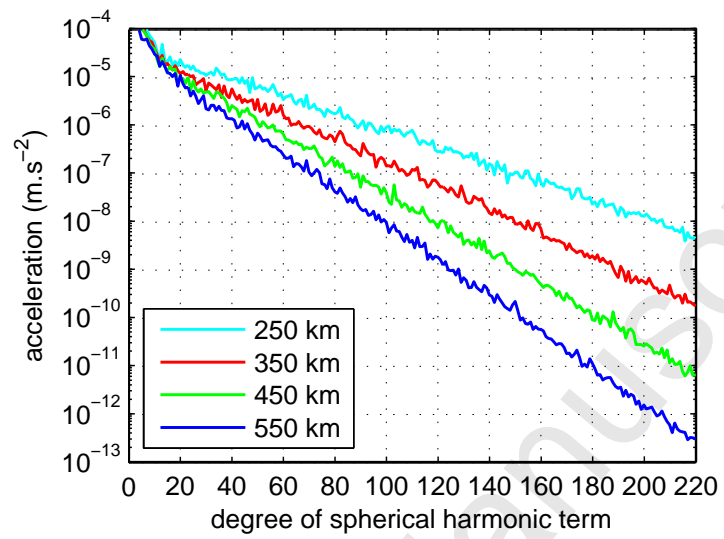
Figure 2



959

960

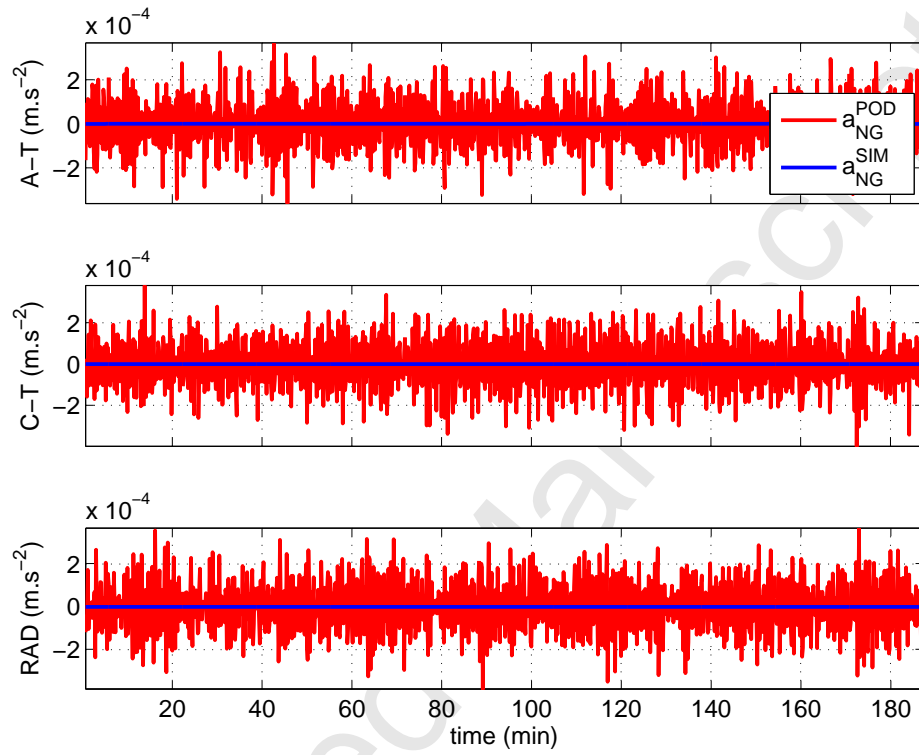
Figure 3



961

962

Figure 4



963

964

Figure 5

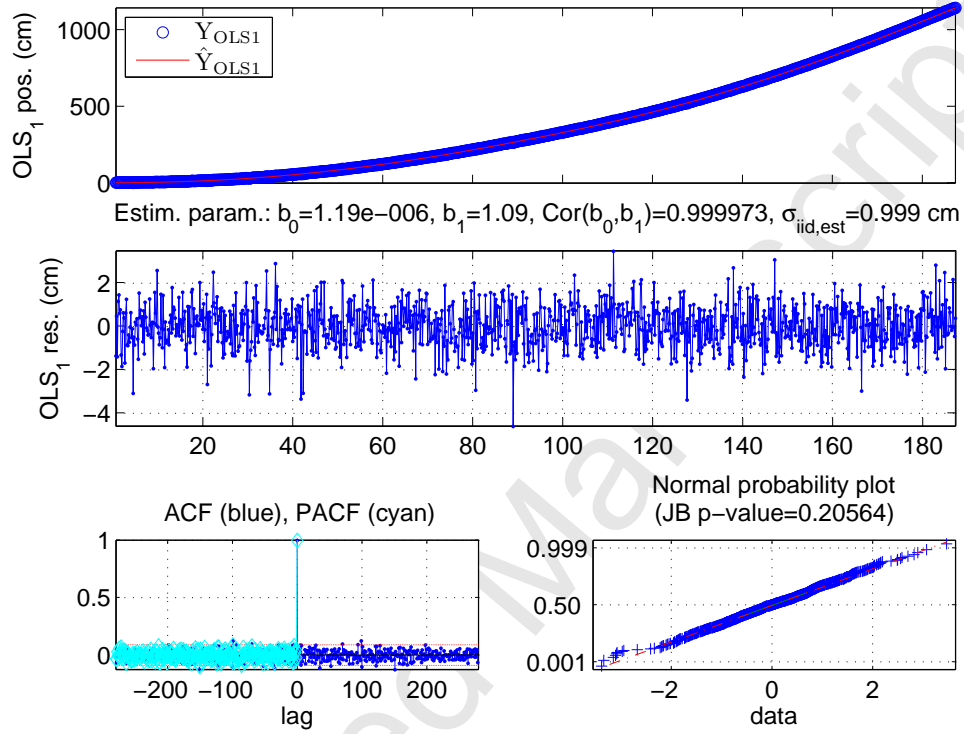
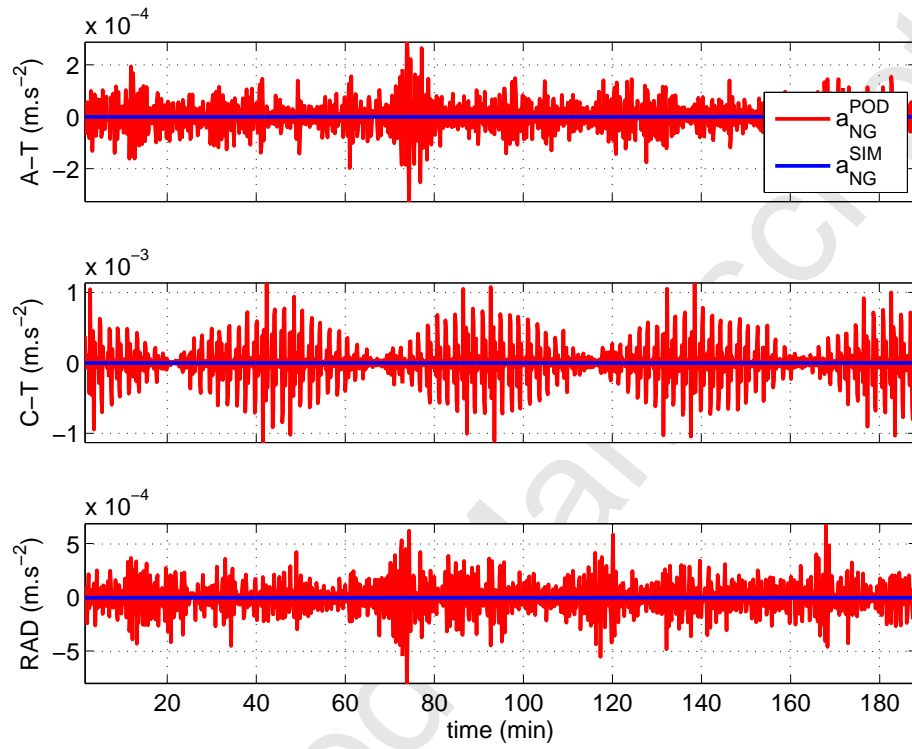


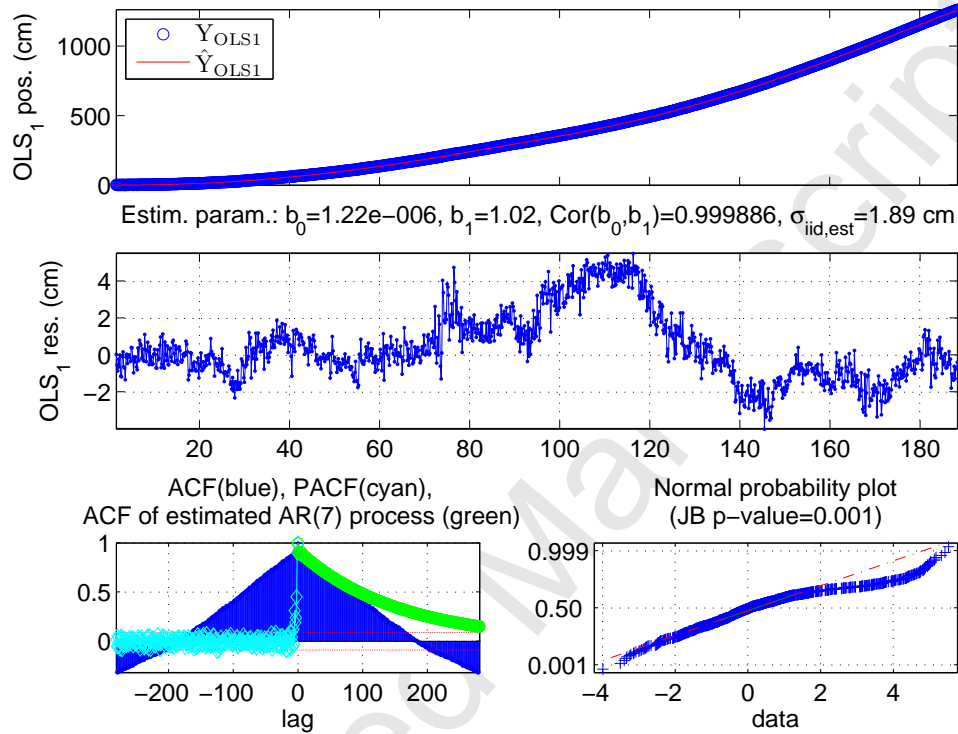
Figure 6



967

968

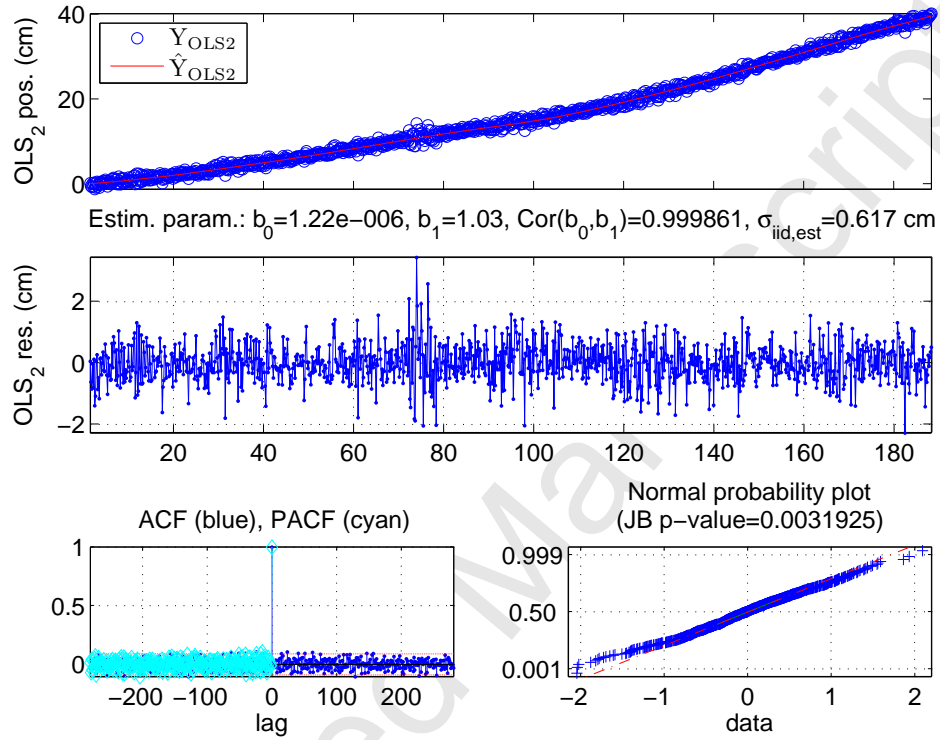
Figure 7



969

970

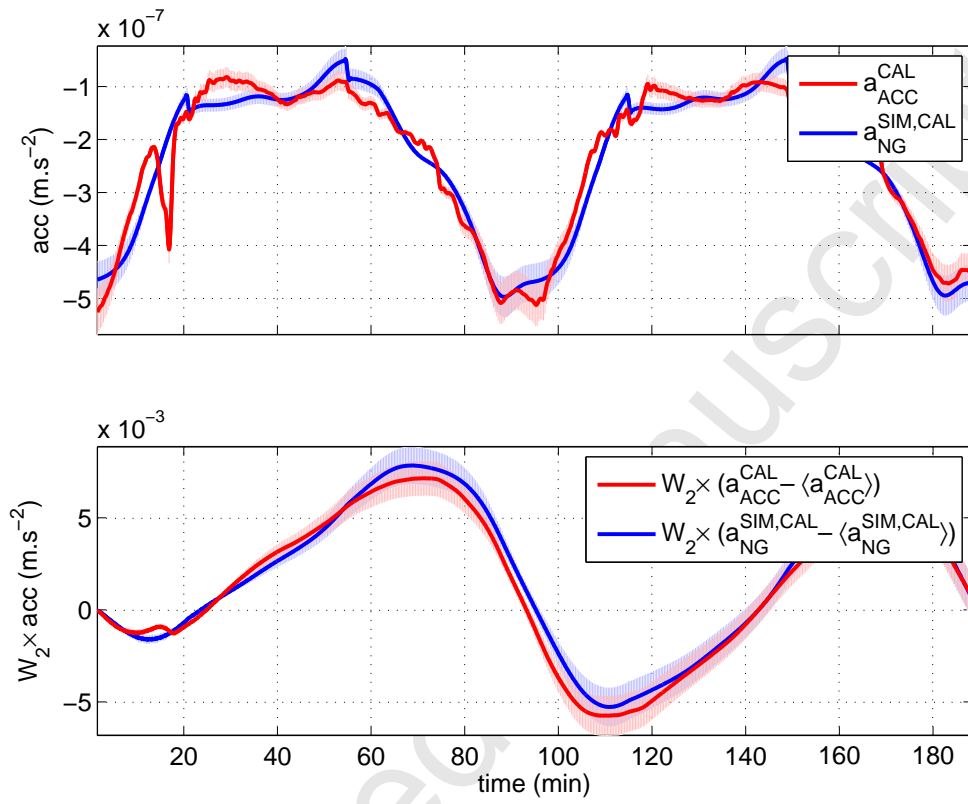
Figure 8



971

972

Figure 9



973

974

Figure 10

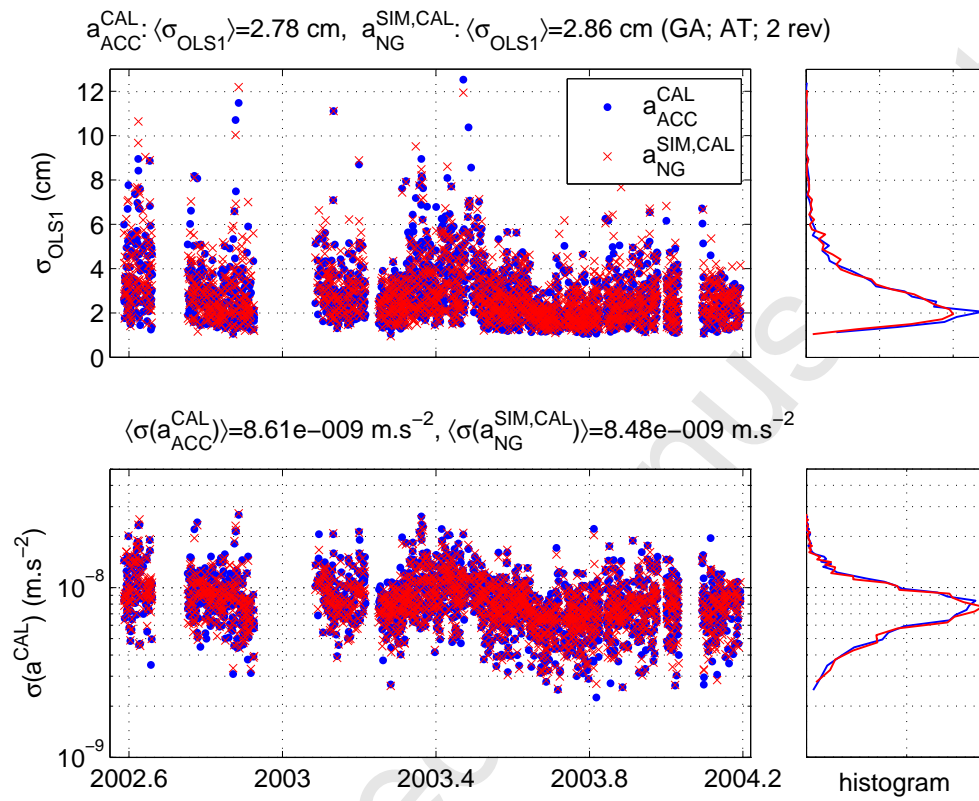
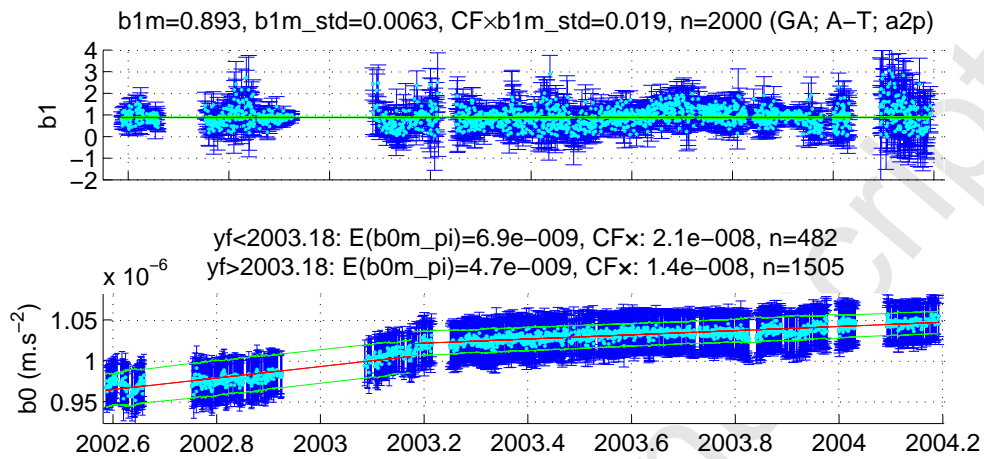


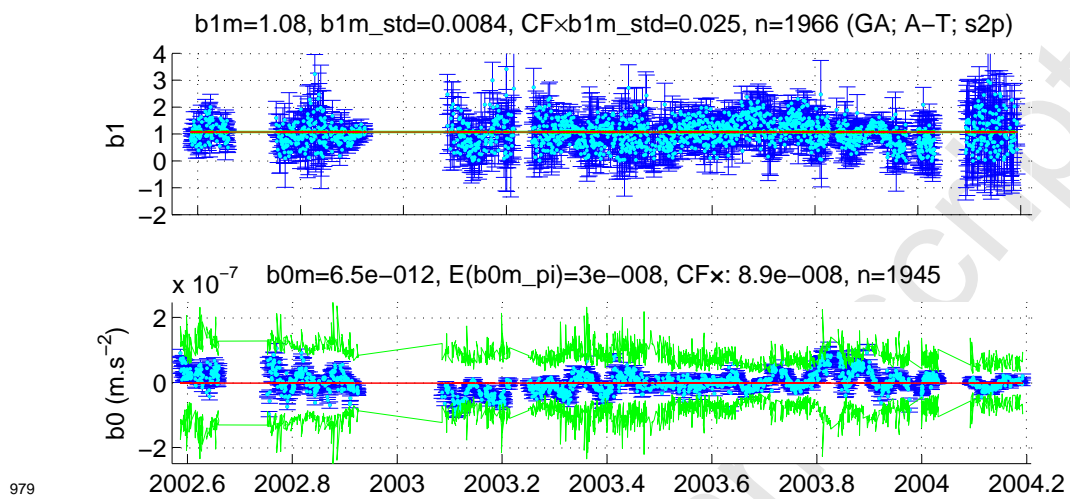
Figure 11



977

978

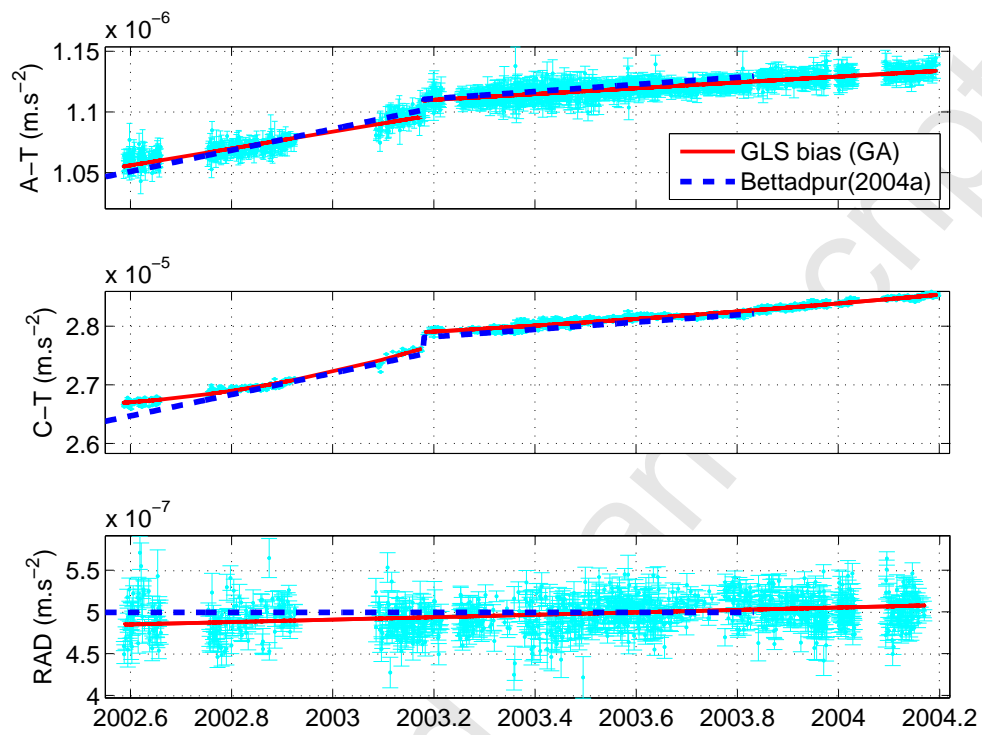
Figure 12



979

980

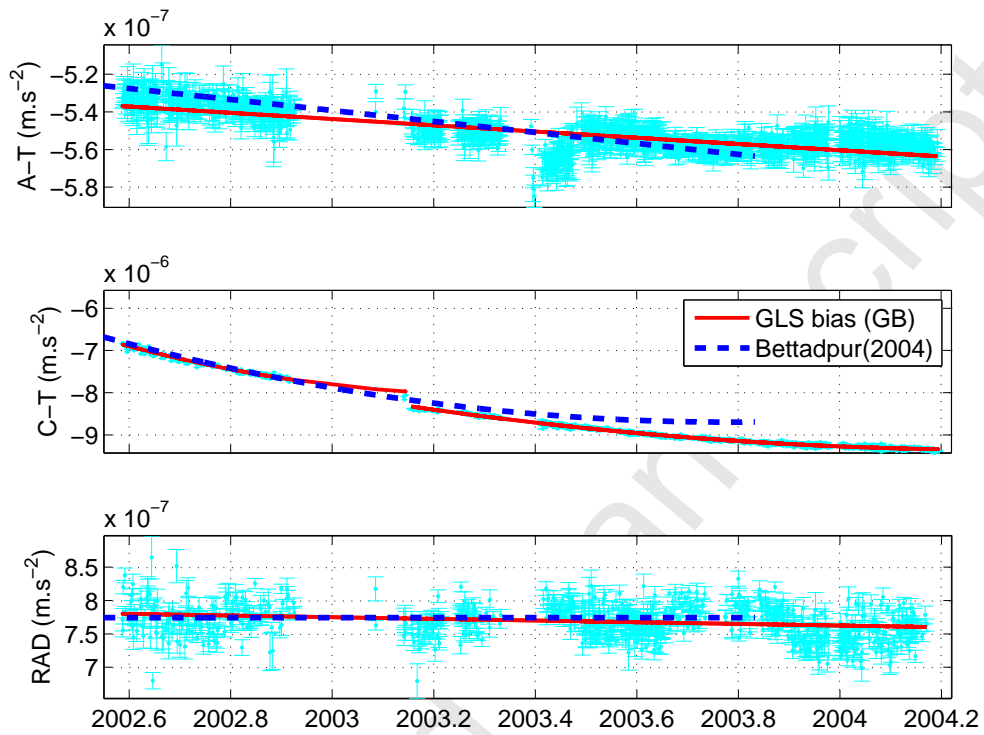
Figure 13



981

982

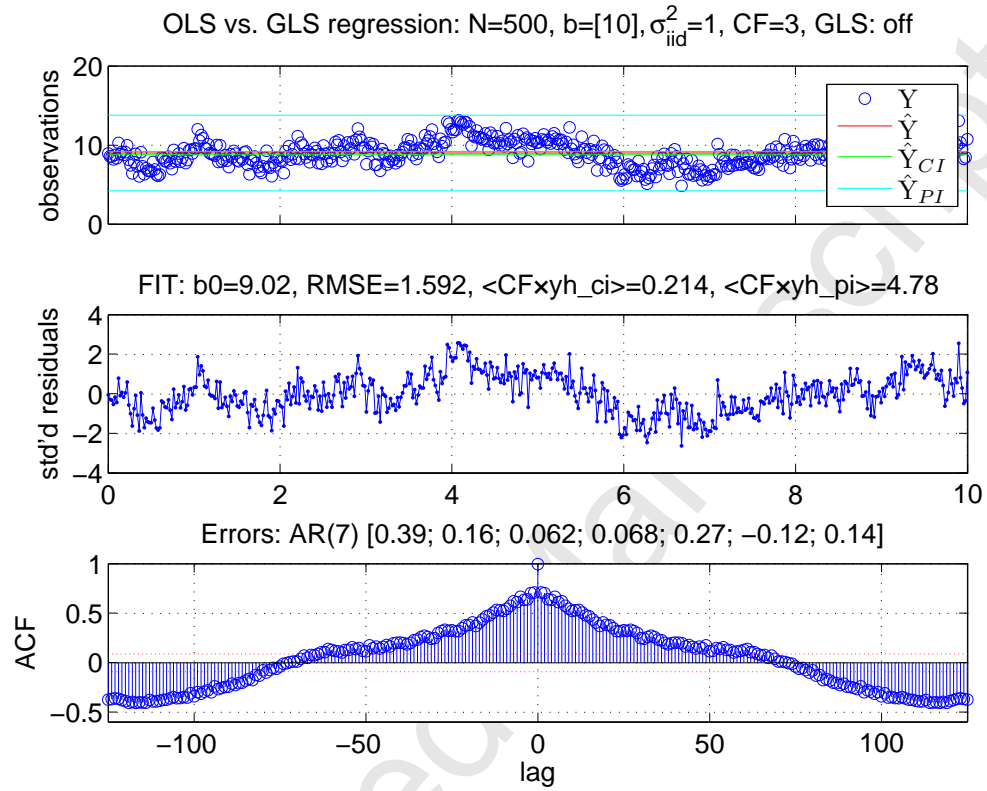
Figure 14



983

984

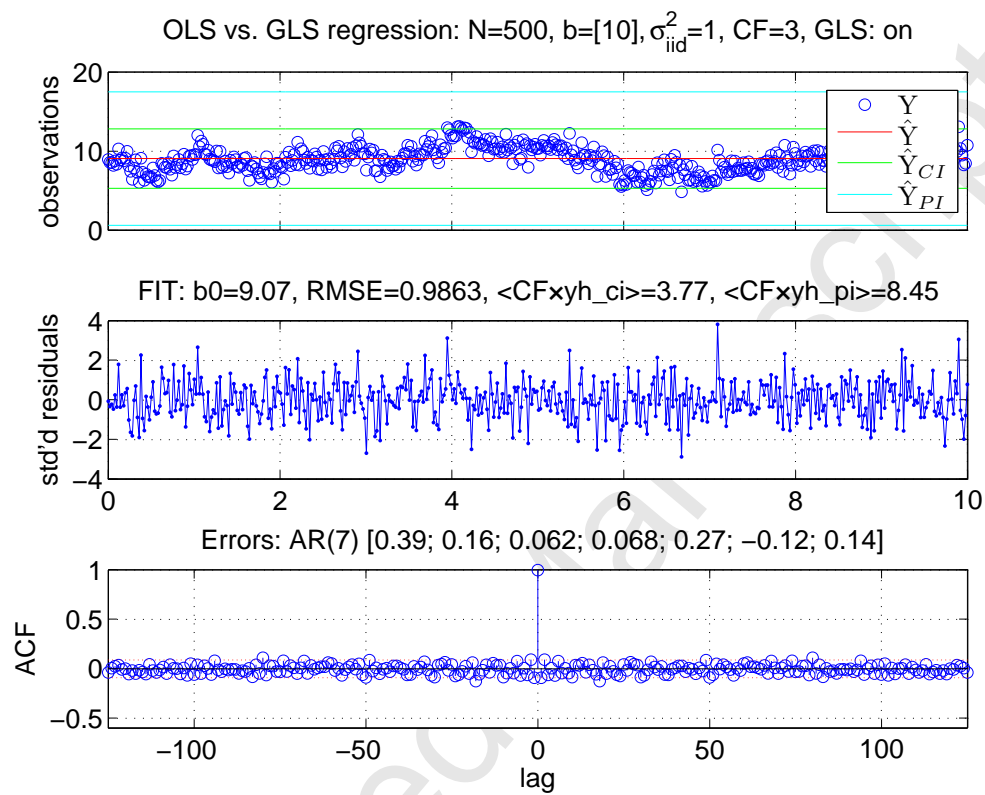
Figure 15



985

986

Figure 16



987

988

Figure 17

gravity model	$\langle \hat{\sigma}_{OLS1} \rangle$ (cm)			$\langle \hat{\sigma}(a_{ACC}^{CAL}) \rangle$ (nm.s ⁻²)		
	A-T	C-T	RAD	A-T	C-T	RAD
EIGEN-5C ⁽¹⁸⁰⁾	3.4	5.3	9.0	7.4	–	20.9
EGM08 ⁽¹⁸⁰⁾	3.5	5.1	9.1	7.5	–	21.1
GGM03C ⁽¹⁸⁰⁾	3.5	5.3	9.9	7.7	–	22.6
GGM03S ⁽¹⁸⁰⁾	3.5	5.3	9.8	7.7	–	22.5
EIG-CH03S ⁽¹⁴⁰⁾	3.5	4.9	9.8	7.6	–	22.1
DEOS-CH ⁽⁷⁰⁾	3.5	6.2	10.7	7.7	–	23.1
EIGEN-5C ⁽⁷⁰⁾	3.5	6.1	10.7	7.7	–	23.5
EGM96 ⁽¹⁸⁰⁾	4.2	20.1	46.3	8.4	–	47.2
GRIM5C ⁽¹²⁰⁾	3.9	18.8	40.5	8.8	–	46.4

Table B.1: Statistical results of selected gravity field models for GRACE A over the period of 1.5 years. The numbers in superscript indicate the degree/order of the model used in our calculations (window of 3 revs., mean of approx. 1000–1400 values).